J. Fluid Mech. (1990), *vol.* 213, *pp.* 479–509
Printed in Great Britain

An experimental investigation of the turbulent structure in a two-dimensional momentumless wake

By J. M. CIMBALA AND W. J. PARK
Department of Mechanical Engineering, The Pennsylvania State University, University Park, PA 16802, USA

(Received 20 January 1989)

Mean velocity profiles have been measured in the wake of a two-dimensional airfoil with and without mass injection through a slit along its rear end. In particular, four cases have been documented: (*a*) a pure wake (no injection), (*b*) a weak wake (some injection), (*c*) a momentumless wake (injection adjusted to provide a thrust which exactly cancels the model's drag), and (*d*) a weak jet (more injection than necessary to cancel the drag). These mean velocity profiles clearly show the difference in momentum deficit for the four cases. When non-dimensionalized, the velocity profiles are self-similar.

Smoke-wire flow visualizations are also presented for both the near wake ($0 < x/d < 30$) and the far wake ($45 < x/d < 75$). The characteristic geometry of large-scale turbulent vortical structures is easily identifiable for the wake and jet cases, while the structures for the momentumless state are neither wake-like nor jet-like. Beyond about 45 diameters downstream, turbulent structures for the momentumless case become quite weak and can barely be observed.

For the momentumless wake at $Re = 5400$, the axial, lateral, and transverse turbulence intensities as well as the Reynolds stress were measured. Similarity of the axial and the transverse turbulence intensities was observed; the overall shape of those profiles is Gaussian except for the very near-wake region. The mean centreline velocity difference decays much faster ($x^{-0.92}$) than the axial turbulent intensity ($x^{-0.81}$). Consequently, the mean shear practically disappears far downstream; the flow becomes nearly isotropic beyond about 45 body diameters from the model. This turbulence behaviour is quite different from that of plane wakes or jets but rather closer to the case of grid turbulence.

1. Introduction

1.1 *Historical overview*

For the case of either a pure jet or a pure wake, the flow far downstream is characterized by the net momentum flux in the streamwise direction. In both cases, as one travels downstream, the momentum flux is independent of streamwise direction x. Of interest here is the case where jet and wake coexist. In particular, if the jet strength is adjusted to balance the wake drag, the net momentum deficit is zero; the flow downstream is known as a momentumless wake. Examples include the wake of a self-propelled body moving at constant velocity. While several studies of axisymmetric momentumless wakes have been reported, there have been very few experimental studies of two-dimensional wakes with the addition of thrust.

Experimentally, axisymmetric momentumless wakes in a non-stratified medium were first investigated by the group of Ridjanovic (1963), Wang (1965) and Naudascher (1965). A circular disk with a coaxial jet in its centre portion was placed in a wind tunnel at Reynolds number based on the diameter of the model, $Re_d = 5.5 \times 10^4$. Naudascher chose the centreline velocity difference, U_d (the difference between the free-stream velocity and the mean centreline velocity) and $(\overline{u'^2})^{\frac{1}{2}}_{\max}$ as appropriate velocity scales; while the radial distance $r_{\frac{1}{2}}$ (the half-width of the axial turbulence intensity profile) and an integral scale L, deduced from the autocorrelation function, were chosen as appropriate lengthscales. He pointed out that the notable difference between the self-preserved profiles for simple jets and wakes and those for the momentumless wake lies in the number of scales necessary to normalize these profiles or describe them. He concluded that the momentumless wake is analogous to elementary turbulent free-shear flows in an initial regime and to decaying homogeneous turbulence in the subsequent shear-free regime. Another similar experiment with coaxial jet injection was carried out by Ginevskii, Pochkina & Ukhanova (1966).

Subsequently, several researchers have carried out more application-oriented experiments by using models which more closely resembled self-propelled vehicles. These included studies of a propeller-driven Rankine-ovoid model by Gran (1973), a propeller-driven slender body and a peripheral-jet model by the group of Swanson, Schetz & Jakubowski (1974), Chieng, Jakubowski & Schetz (1974), and Schetz & Jakubowski (1975). Schetz & Jakubowski investigated the flow fields behind slender body models of three different types at $Re_d = 6 \times 10^5$. They observed that the wake development of a blunt body, driven by a jet to yield a zero momentum wake (as studied by Naudascher), was significantly different from the wake of a slender, streamlined body driven by a peripheral jet. The wake decay rate, U_d/U_∞ with x/d, was more rapid for the jet-driven body than for the propeller-driven body. The width of the pure drag body wake was narrower than the jet model wake, which was in turn narrower than the propeller model.

More recently Higuchi (1977) used a circular jet injection tube so as to produce drag by the turbulent boundary layer on the outer surface of the tube model at $Re_d = 2.7 \times 10^4$. To study the effect of initial conditions on the far downstream behaviour, Higuchi artificially thickened the boundary layer by attaching rims on the tube model. He observed that the wake relaxes into the final decay law sooner for this case; the relaxation length in which the matched injection wake reached its final stage depended on the initial conditions. For this type of momentumless wake, a good review article can be found in Schetz (1980).

There have been several studies of axisymmetric momentumless wakes in stratified media; see Park (1989) for a detailed review of these.

There have been some experimental studies of two-dimensional wakes with the addition of thrust, the major objective being to reduce the aerodynamic drag of a bluff body by means of base bleed. The effect is similar to that of a splitter plate located behind a bluff body which was first investigated by Roshko (1954). Experimentally, base bleed in subsonic flow was first studied by Wood (1964, 1967). He used an airfoil-shaped model with a blunt rear portion at $Re_c \approx 1.0 \times 10^6$; air was exhausted through a slit spanning the rear of the model. He found that base bleed reduces drag by delaying the onset of instability in the separated shear layers. Bearman (1966) further investigated the effect of base bleed on the development of vortex streets behind a two-dimensional model at $Re_{d_1} = 4.1 \times 10^4$. He observed that with sufficiently large bleed quantity the regular Kármán vortex street pattern

disappeared behind the body, but appeared further downstream. Again the results are quite similar to the addition of a splitter plate, as discussed by Wood. However, neither Wood nor Bearman supplied enough thrust to achieve zero overall drag.

To produce an inhomogeneous turbulent flow without mean velocity gradients, on the other hand, Townsend (1956) utilized a two-dimensional composite grid consisting of two metal angles and two sheets of fine wire mesh. By controlling the gap (i.e. undisturbed opening) between the two metal angles, the mean pressure drop over the whole arrangement was made equal to the pressure drop of the mesh. He thus obtained an inhomogeneous turbulence flow with plane symmetry; the turbulent intensity profiles were roughly self-preserved and Gaussian-like. The decay rate of turbulent intensity in his flow was rather more rapid than that of isotropic turbulence.

Mobbs (1968) performed a similar experiment to that of Townsend. He included the measurement of the intermittency factor to study the entrainment process at the interface between non-turbulent and virtually homogeneous turbulent fluid in the absence of mean velocity gradients. He observed that the intensity ratios u'/v' and v'/w' gradually approached unity (i.e. isotropy). He documented the variation of the scale of the intermittent zone, L_γ, with distance x from the composite grid. The flow field generated by a composite grid is undoubtedly a sort of two-dimensional momentumless wake; however, the detailed evolutionary history of the mean flow characteristics and the distribution of Reynolds stress were not documented by Townsend (1956) or Mobbs (1968).

Very recently, some two-dimensional momentumless wakes have been studied by Williams & Amato (1988) in a water channel. Namely, zero momentum wakes have been obtained by periodic suction and blowing through small holes at the trailing edge of a circular cylinder model. This approach differs from the standard base bleed techniques in that no net mass is added to the wake.

We now turn our attention to the theoretical and numerical approaches to the momentumless wake flow problem. Birkhoff & Zarantonello (1957) first discussed analytically the linearized solution for the far downstream portion of momentumless wakes by the classical means of dimensional analysis. A similar argument was presented for wakes, jets, and momentumless wakes by Tennekes & Lumley (1972). They assumed that the width of the wake will grow like x^n, while the maximum velocity defect will decay like x^{n-1}. Unfortunately, the exponent n becomes indeterminate for the zero momentum wake; hence it is not predictable analytically unless one resorts to some type of eddy-viscosity assumption. Both pairs of researchers adopted an assumption of constant eddy viscosity through the flow field to obtain results from the momentum relationship. One of their approximations leads to $n = \frac{1}{4}$ for the two-dimensional case and $n = \frac{1}{5}$ for the axisymmetric case, but experiments are not available for the two-dimensional case.

For the axisymmetric case, this zero-equation turbulence model was directly tested by Ginevskii, Ukhanova & Pochkina (1972) and Ko (1973), and a modified version was developed by Schetz & Stanley (1972), while Kubota (1975) developed a more inclusive version of the model by retaining higher-order terms. However, these calculations with Prandtl's hypothesis and the mixing-length theory show, in general, poor agreement with experimental data.

Various turbulence models have been applied subsequently for more accurate prediction of momentumless wakes. All of the following numerical simulations, however, have been done exclusively on axisymmetric cases, because no comprehensive experimental data, which are useful to determine relevant constants in

higher-order-stress closure models, are available for two-dimensional cases. One-equation turbulent models were used by Gran (1974) and Swanson *et al.* (1974) while Jubota (1975) and Hassid (1980) employed turbulent energy-dissipation (κ–ϵ) models. These κ–ϵ models agreed fairly well with most of the experimental data discussed above.

Lewellen, Tesks & Donaldson (1973, 1974) applied Donaldson's second-order-stress closure model to Naudascher's and Schetz *et al.*'s data. Another type of second-order-stress turbulence model was discussed by Finson (1975); he adopted the ideas of Rotta (1951), Donaldson (1972), and Hanjalic & Launder (1972) to solve for momentumless wakes. Finson obtained a decay law which agrees closely with the results of Naudascher's experiment by taking his constants from experiments on homogeneous grid turbulence. More recently, Shashmin (1983), and Korobko & Shashmin (1985) also used a second-order-closure Reynolds stress model. Meanwhile there were other attempts to investigate momentumless wakes by direct numerical simulation (i.e. the pseudospectral method). Orszag & Pao (1973), and Metcalfe & Riley (1980) are examples. They directly analyzed the three-dimensional Navier–Stokes equation using fourier transformations without any turbulence closure assumption.

1.2. *Objective*

As discussed earlier, there have been no comprehensive experiments to date on two-dimensional momentumless wakes. If the coefficients for turbulence models are determined by empirical fit of axisymmetric data, these same coefficients will not work for two-dimensional flows. Therefore, a complete set of accurate two-dimensional momentumless wake data is required. The primary objective of this investigation is thus to experimentally measure the rapid decay of turbulence downstream of a two-dimensional momentumless body. The emphasis is focused on measurements of mean velocity profiles and turbulence intensities as well as smoke-wire flow visualizations at several downstream locations in the wake to document the geometry and scale of the turbulent structure. Three-dimensional effects in the two-dimensional momentumless wake are also discussed briefly.

2. Experimental set-up

2.1. *Wind tunnel*

The flow-visualization experiments as well as the hot-wire measurements were conducted in an open-return subsonic low-turbulence wind tunnel. The test section is 0.3×0.97 m in cross-section and 2.4 m long. Free-stream speed is variable from 1.0 to 15 m/s. The contraction and settling chamber have been carefully designed according to turbulence-management suggestions of Loehrke & Nagib (1972) and provide background turbulence intensity of order 0.1 % at a free-stream velocity of 5 m/s. This facility is unique in that the test section is fully rotatable about the x-axis, which permits flow visualization from any desired orientation. The rectangular (3.2:1) test section is ideal for studying two-dimensional wakes or jets. To compensate for free-stream blockage due to boundary layers along the walls, the bottom plate of the test section is diverged at an angle of about 0.5°.

A temperature gradient may produce totally unrealistic results owing to the sensitive temperature dependency of hot-wire anemometry at low free-stream velocities. To improve the wind-tunnel performance in the presence of appreciable temperature stratification in the room, a mixing fan assembly was installed just in

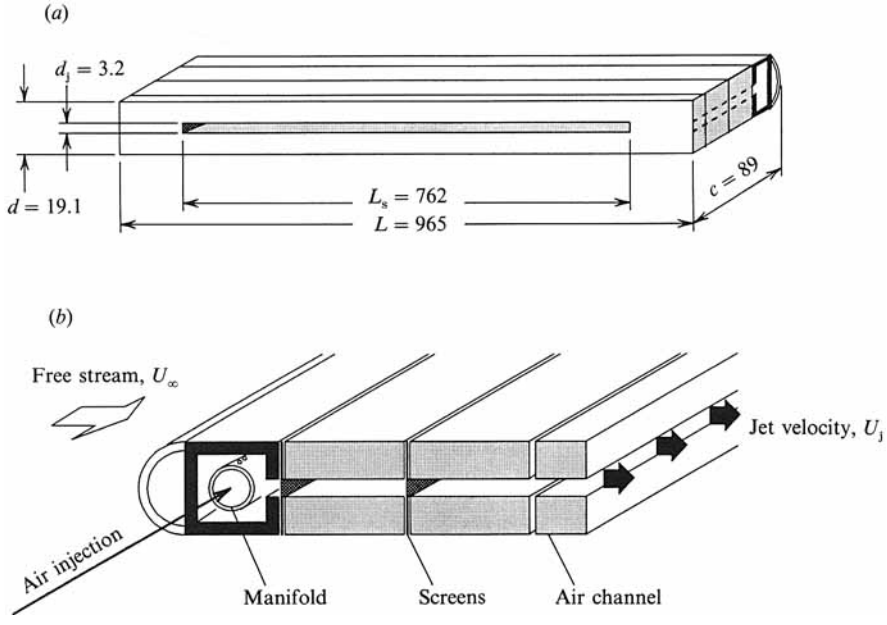

FIGURE 1. Two-dimensional momentumless-wake model: (*a*) overall dimensions in mm. (b) details.

front of the wind-tunnel air-intake area so as to mix the room air from top to bottom. These mixing fans proved to be very effective (see Cimbala & Park 1989*a*).

2.2. *Two-dimensional model and air supply system*

To provide enough thrust to balance the drag, a controlled amount of air has to be injected at the trailing edge of the two-dimensional model parallel to the free stream. For this purpose, house air with a supply pressure of approximately 450 KPa was introduced into the air supply control system. Steady air flow was maintained by regulating the pressure upstream of the two-dimensional model.

The two-dimensional air jet-injection model was composed of four parts: the leading edge, the manifold, the hollow square cylinder as a settling chamber, and the air channel. Overall, the model has an airfoil shape with a blunt trailing edge. The aspect ratio of the two-dimensional model was 51 and the jet-injection slit covers about 80% of the total model span. Details and dimensions of the model are shown in figure 1. Considerable effort was devoted to the design of a two-dimensional uniform velocity injection system to provide thrust, as described in Park (1989). Velocity non-uniformities of around $\pm 2\%$ were measured over the entire span, and of less than $\pm 1\%$ were measured in the middle 0.3 m span of the model. Free-stream velocity U_∞ was chosen to be 4.2 m/s, which is the speed at which the free stream is most uniform. The Reynolds number based on the diameter of the model was $Re_d \approx 5400$.

2.3. *Instrumentation and data acquisition system*

Wind-tunnel free-stream velocity was measured with a Pitot-static probe and an electronic pressure transducer. The local barometric pressure was continuously monitored by an electronic absolute pressure transducer. The mean temperature of the test section was monitored at the exit of the test section with two thermister probes. These two readings were averaged over 10 s and implemented into the mean

flow data reduction routine. Mean velocity profiles were obtained with a single hot-wire probe, mounted on a two-direction traversing mechanism with stepper motor controller. Turbulence fluctuating velocities were measured with a dual-sensor hot-wire probe. A direct hot-wire calibration scheme, which utilizes a single equation for velocity as a function of hot-wire voltage, ambient temperature and ambient pressure, was employed. Details of this technique can be found in Cimbala & Park (1989*b*).

The positioning of the probe as well as the data sampling were controlled by laboratory microcomputer and digital data acquisition system. Details of the experimental set-up can be found in Park (1989).

3. Flow-visualization results

With the free-stream velocity U_∞ fixed at 4.2 m/s, the Reynolds number based on model diameter was 5400. Jet injection velocity was varied to produce four typical flow conditions: (*a*) a pure wake (no jet injection), (*b*) a weak wake (jet injection not sufficient to overcome the body drag, (*c*) a momentumless wake (jet injection adjusted exactly to balance the drag), and (*d*) a weak jet (more jet injection than necessary to overcome the drag).

Smoke-wire flow visualizations were obtained along the model centreline at seven streamwise positions. By always mounting the smoke wire just upstream of the region of interest, the often confusing integration effect of streakline visualization was eliminated (Cimbala 1984; Cimbala, Nagib & Roshko 1988). Results for the smoke wire mounted at $x/d = 0$, 15, 45 and 60 are shown in figures 2–5 respectively.

In figure 2, with the flow from 0 to 15 diameters visualized, the characteristic large-scale Kármán-type vortex pattern is clearly identifiable for both the pure wake (photograph *a*) and the weak wake (photograph *b*). For the pure wake at about $x/d = 5$, the shedding frequency can be directly estimated at approximately 50 Hz based on the scaled distance between two vortices in photograph (*a*) and the mean velocity measured at the half-width of the wake at $x/d = 5$. The momentumless wake (photograph *c*) and the weak jet (photograph *d*) appear to have wake-like structures at their edges but the pattern is quite disorganized compared to the upper two photographs.

In figure 3, the view is from 15 to 30 diameters, with the smoke wire mounted at $x/d = 15$. Again, the prominent structures for the pure wake and weak wake are clearly wake-like, while those of the weak jet have become distinctly jet-like in character. The momentumless wake (photograph *c*) at this location contains turbulent structures which are neither wake-like nor jet-like, but instead seem to burst out into the free stream at random intervals. This type of structure was also observed by Higuchi (1977) with a thin laser sheet in a non-stratified medium, and by Gilreath & Brandt (1983) with a shadowgraphic technique in a stratified medium for axisymmetric momentumless wakes.

In figure 4, the view is from 45 to 60 diameters. The structures for the pure wake, the weak wake, and the weak jet have evolved in the streamwise direction maintaining their respective characters. One can easily notice the very rapid decay of large structures for the momentumless wake (photograph *c*); beyond 45 diameters downstream, large structural motion for the momentumless wake is substantially damped. From about this distance downstream, the turbulence core region seems to shrink compared with the corresponding photograph at the previous location; this fact supports visually the experimental observation of Mobbs (1968), i.e. the

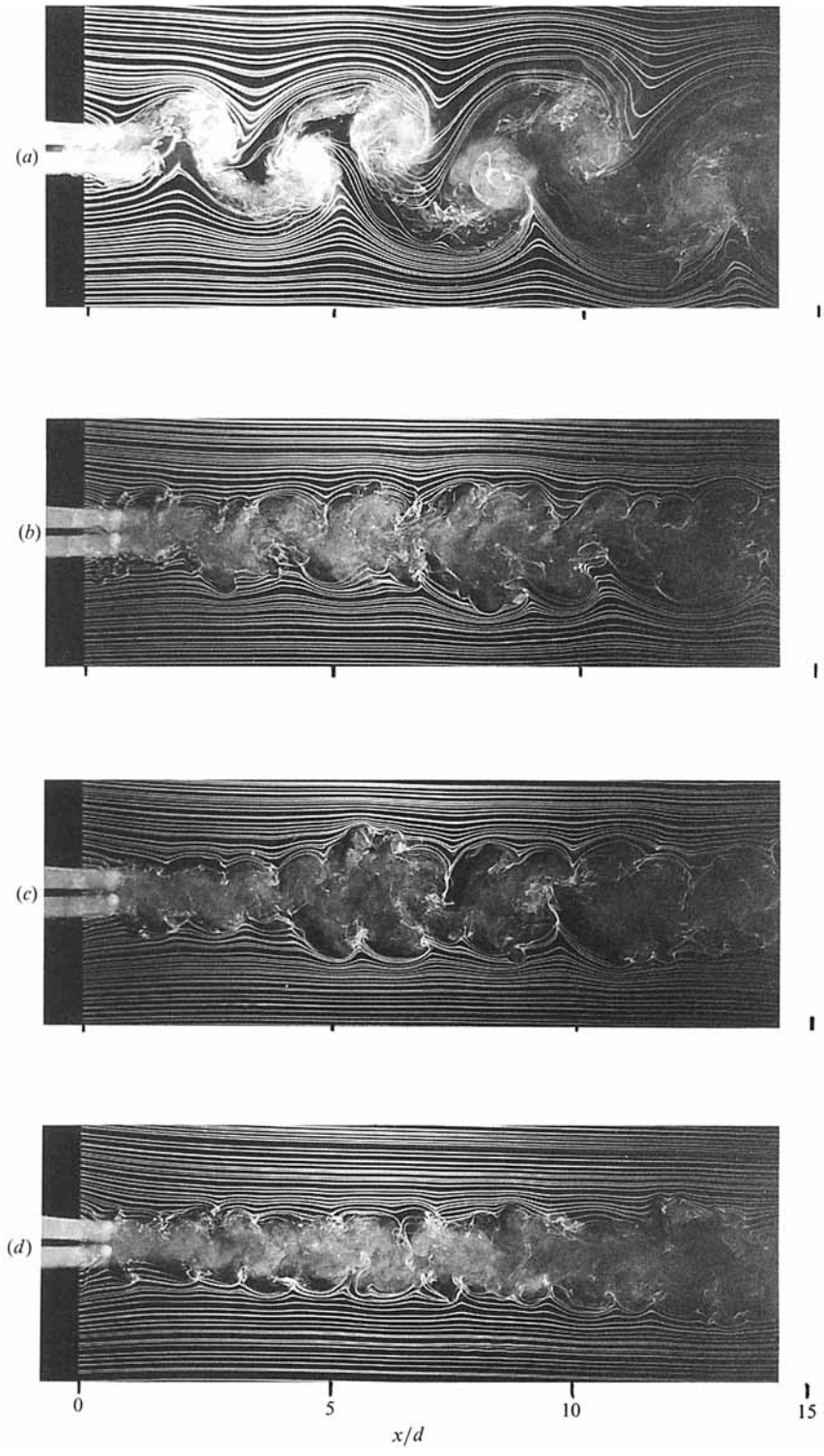

FIGURE 2. Flow visualization at $Re = 5400$, smoke-wire at $x/d = 0$: (*a*) a pure wake, (*b*) a weak wake, (*c*) a momentumless wake, (*d*) a weak jet.

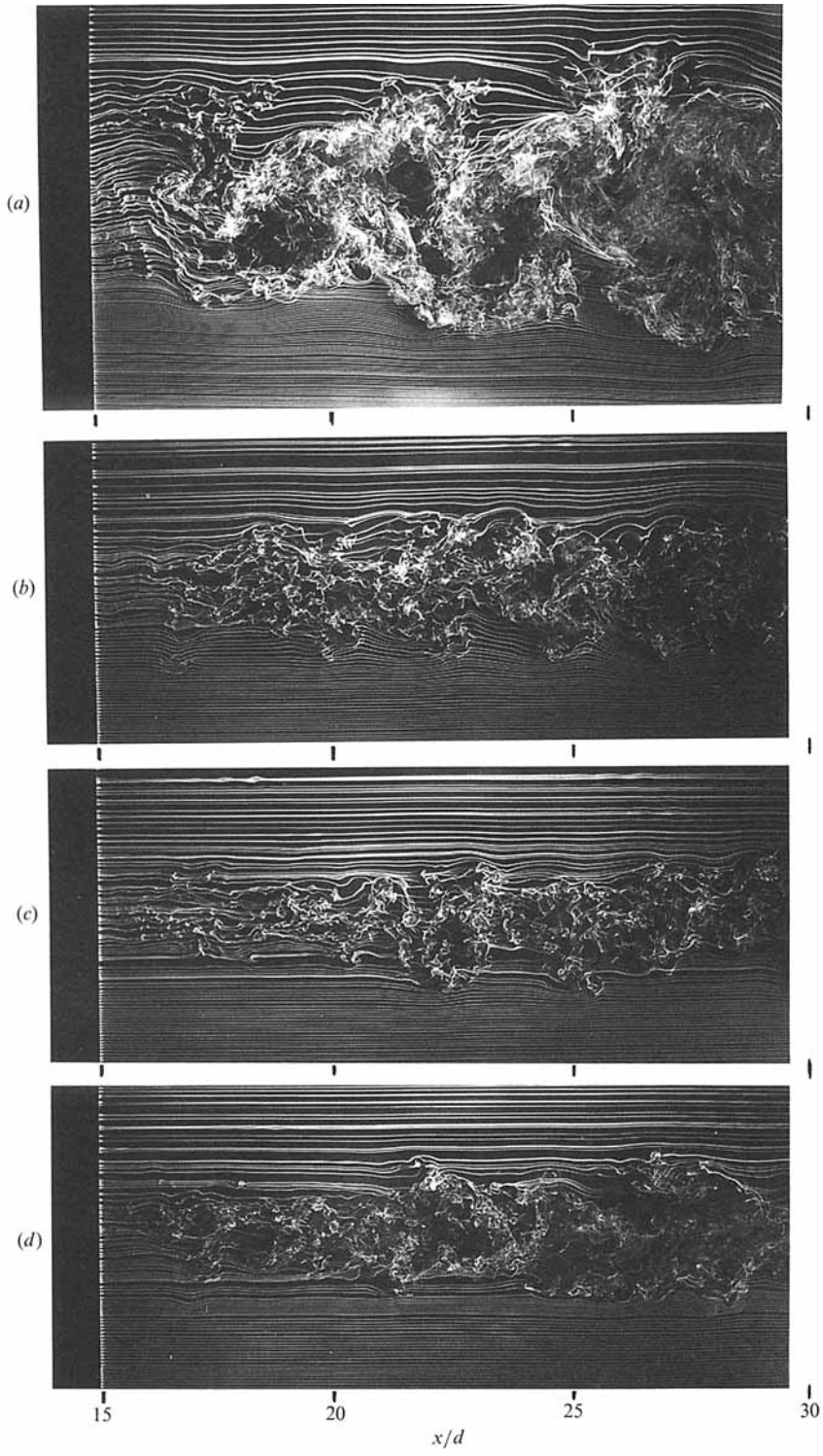

FIGURE 3. Flow visualization at $Re = 5400$, smoke-wire at $x/d = 15$: (*a*) a pure wake, (*b*) a weak wake, (*c*) a momentumless wake, (*d*) a weak jet.

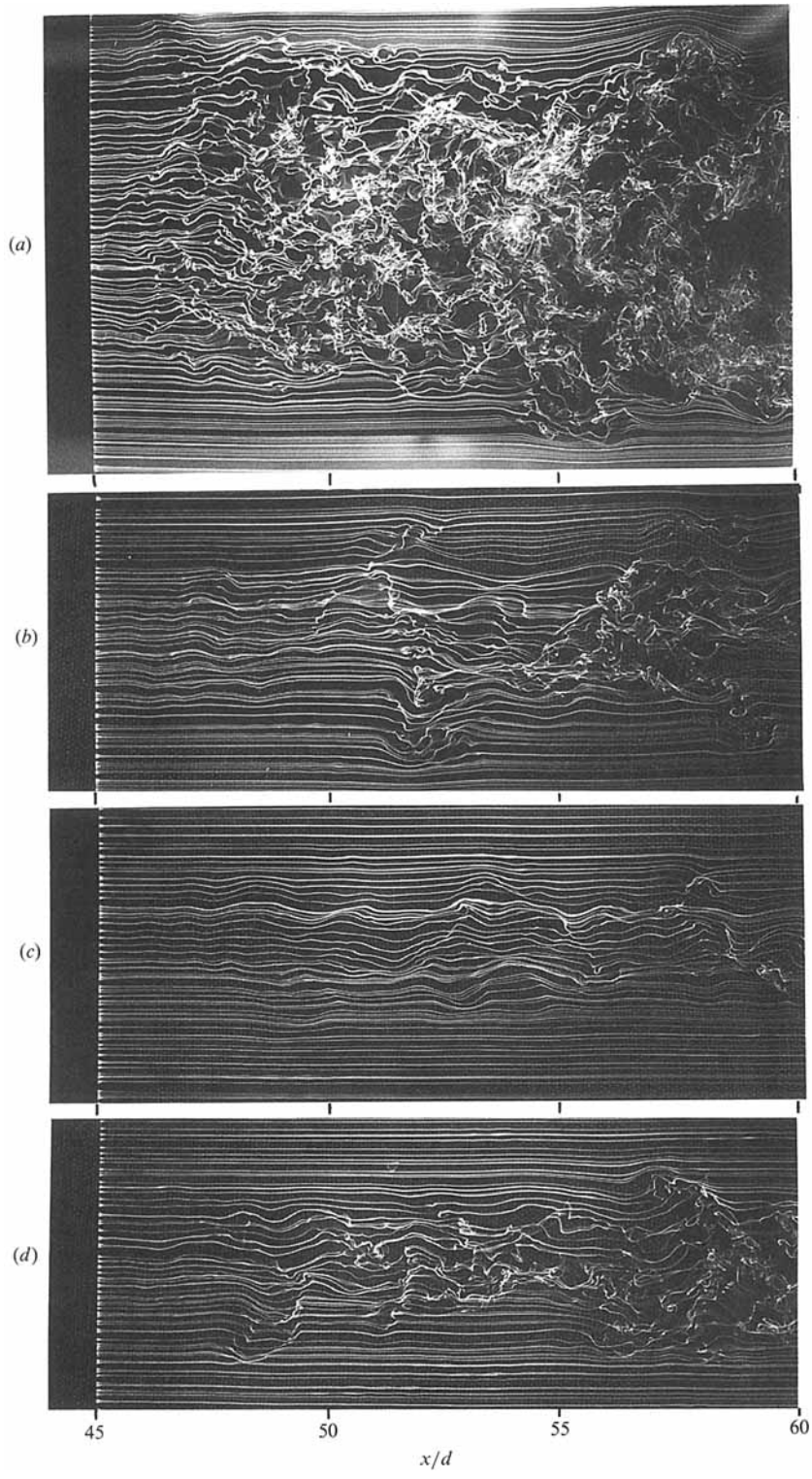

FIGURE 4. Flow visualization at $Re = 5400$, smoke-wire at $x/d = 45$: (*a*) a pure wake, (*b*) a weak wake, (*c*) a momentumless wake, (*d*) a weak jet.

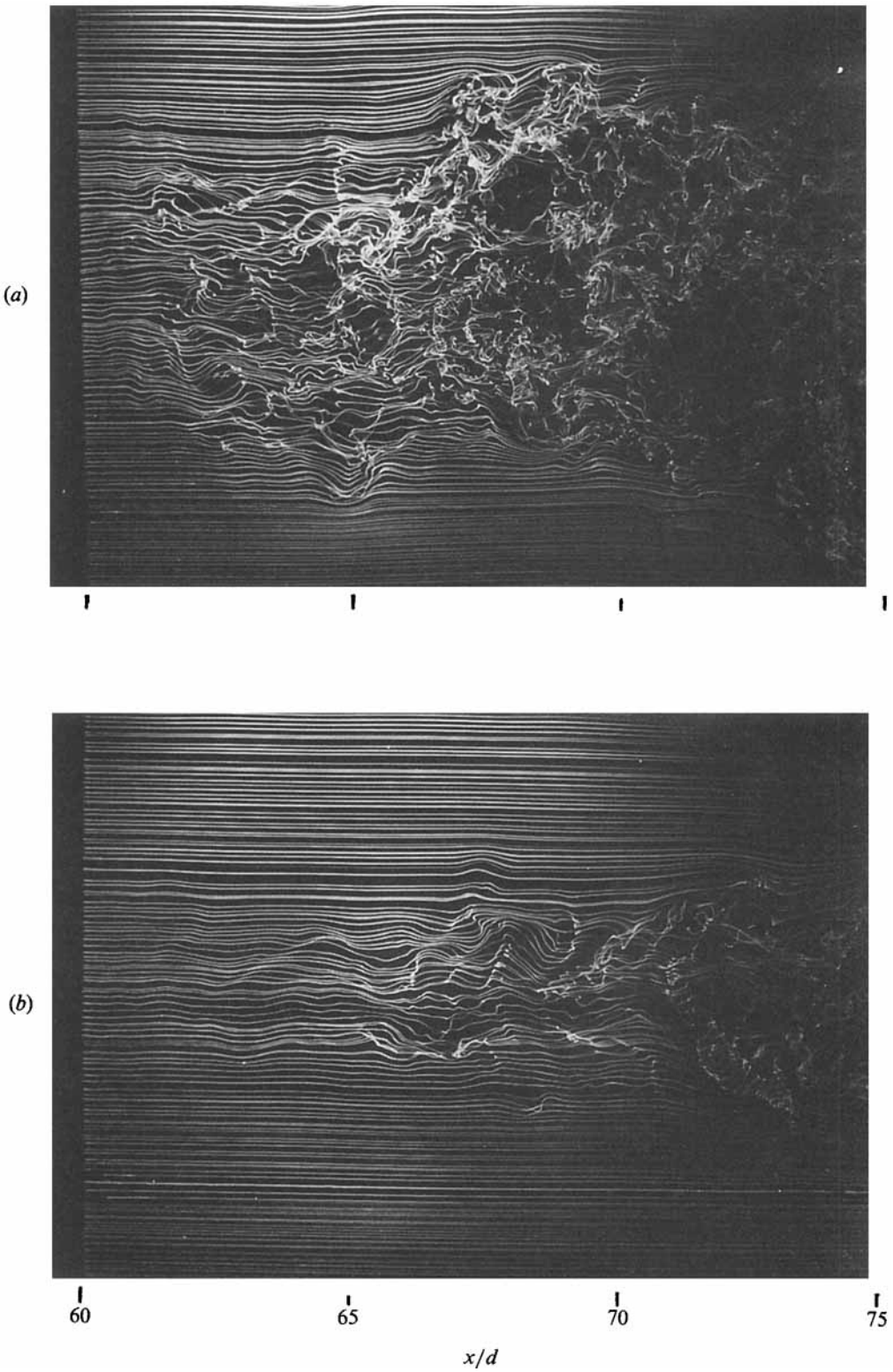

FIGURE 5(a, b). For caption see facing page.

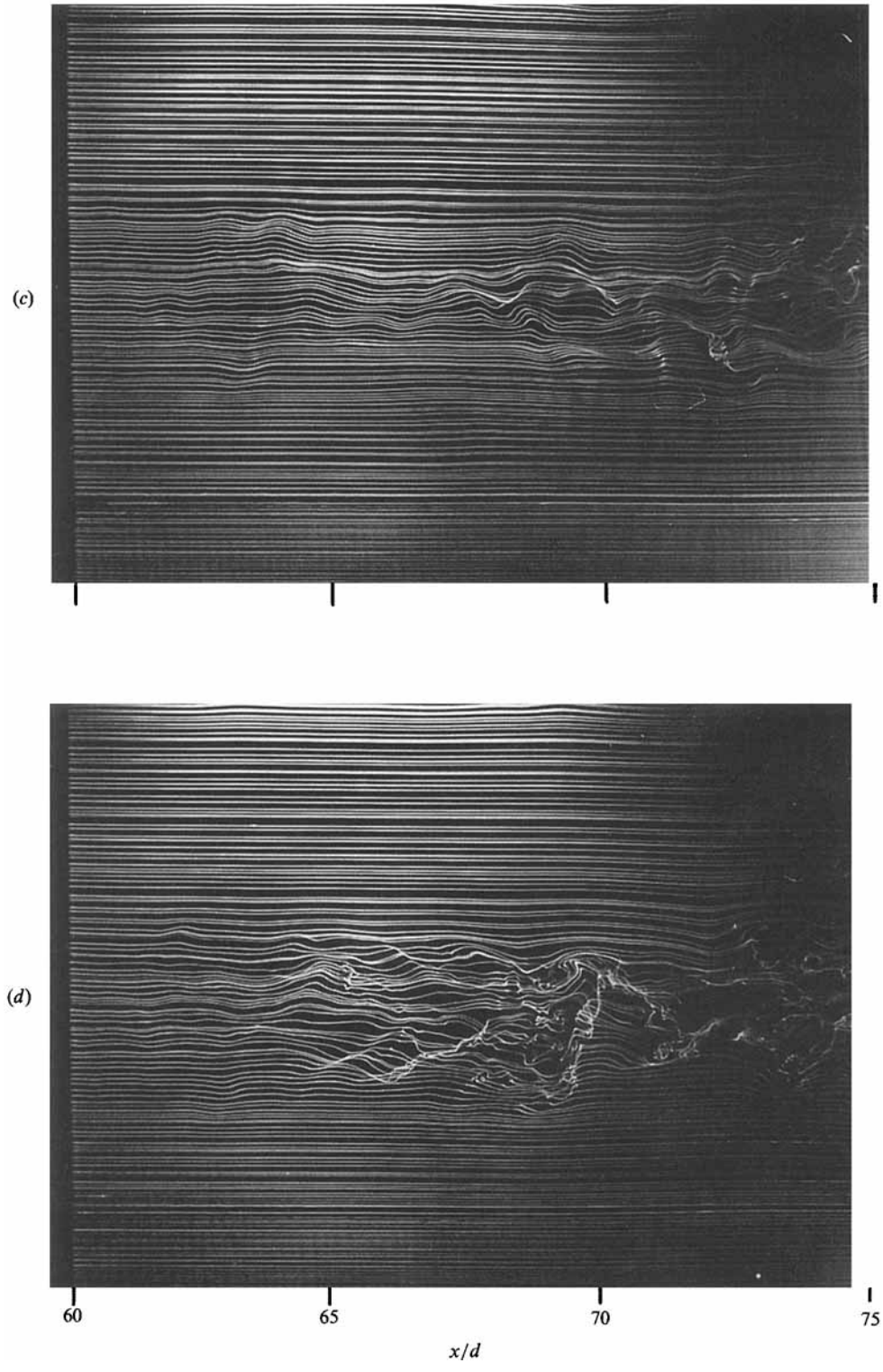

FIGURE 5. Flow visualization at $Re = 5400$, smoke-wire at $x/d = 60$: (*a*) a pure wake, (*b*) a weak wake, (*c*) a momentumless wake, (*d*) a weak jet.

contraction of the turbulence region (in the sense of width of intermittent zone) in his shear-free inhomogeneous turbulence flow.

Figure 5 shows the flow fields far downstream (from $60 < x/d < 75$). By this streamwise distance, the widths of the wakes have grown significantly with a corresponding increase in the scale of the large turbulent vortical structures. For the pure wake and weak wake (photographs *a* and *b*), wake-like structures are still observable but the scale of the large Kármán-type vortices is at least twice that of the near-wake structures. This is analogous to the increase in scale of large-scale structures observed by Cimbala *et al.* (1988) in the far wakes of two-dimensional circular cylinders and porous flat plates. Photograph (*d*) shows the weak-jet case. Although much weaker than those closer to the body, characteristic large-scale jet-type structures are identifiable. The weak-jet case seems to have grown much more slowly than either of the wake cases, but again the scale (i.e. the streamwise distance between large structures) is of order twice that of the near-wake structures. Finally, the momentumless case (photograph *c*) has only small random fluctuations, indicating that the wake turbulence has all but decayed completely. Notice also that the width of the momentumless wake is much smaller than the other cases, particularly the pure-wake case. All of these qualitative observations agree with the quantitative hot-wire measurements to be discussed later.

4. Hot-wire measurements

4.1. *Mean velocity profiles*

Mean velocity profiles along the model centreline were measured with a single hot-wire probe at eight streamwise stations from 0 to 75 diameters downstream of the model. At each downstream station, 40–60 sampling points were scanned in the vertical y-direction. Data were sampled at 2000 Hz at each sampling point and averaged over a period of 20 s for the finite-momentum-defect (or excess) cases. Because the relative magnitude of the centreline velocity difference of the momentumless wake is much smaller than those of finite-momentum-defect cases, it was necessary to average over a longer time (50 to 150 s).

To achieve a momentumless state at the fixed free-stream velocity, several mean velocity profiles with various air-injection pressures were evaluated. For the four typical flow conditions, momentum thicknesses θ were calculated by numerical integration of the time-averaged mean velocity profiles, i.e.

$$\frac{\theta}{d} = \int_{-\infty}^{+\infty} \frac{\bar{u}}{U_\infty}\left(1 - \frac{\bar{u}}{U_\infty}\right) \mathrm{d}\left(\frac{y}{d}\right). \tag{4.1}$$

Values of θ/d and the jet injection pressure for each of the four cases are shown in table 1. By careful adjustment of the jet pressure, we were able to achieve near zero momentum. As shown in table 1, column (*c*), θ/d was less than 0.003 for all streamwise stations beyond 5 body diameters. Momentum thicknesses for other cases are also nearly invariant along the streamwise direction x beyond the near-wake region, i.e. beyond about 15 (for weak-wake and weak-jet cases) to 45 (for the pure-wake case) diameters downstream. For finite-momentum-defect (or excess) cases, these values show somewhat larger deviation, partly because the blockage effect of the two-dimensional model was not considered. Our weak wake and weak jet have approximately the same magnitude of θ/d but opposite signs.

Tennekes & Lumley (1972) argue that the presence of a non-zero momentum

Flow characteristics ...	(*a*) pure wake	(*b*) weak wake	(*c*) momentumless wake	(*d*) weak jet
Jet pressure (KPa) ...	0	110	140	170
x/d	θ/d	θ/d	θ/d	θ/d
0.15	0.161	−0.075	−0.167	−0.225
5	0.197	+0.092	−0.016	−0.094
10	0.232	+0.107	+0.000	−0.080
15	0.251	+0.098	−0.001	−0.097
30	0.313	+0.107	−0.001	−0.106
45	0.366	+0.127	+0.001	−0.104
60	0.364	+0.100	−0.003	−0.113
75	0.349	+0.115	−0.001	−0.117

Table 1. Summary of momentum thickness (θ/d)

component dominates the momentumless component of the wake. In other words, even a small mismatch in momentum injection at the body will cause the velocity profiles far downstream to appear either jet-like or wake-like, depending on the sign of the mismatch. This argument is supported by the present experiments. Indeed, this behaviour was used to our advantage when establishing the momentumless wake condition! It was observed that the momentumless wake profile (with four inflection points, one maximum, and two minima) could be suddenly shifted to either a totally wake-like or totally jet-like profile (with a single minimum or maximum and only two inflection points) by changing the pressure slightly (less than 5 KPa). The momentumless state was thus easily verified by the mean velocity profile, and could be sustained indefinitely so long as the supply pressure and free-stream velocity were held constant.

Figure 6 shows mean velocity profiles for the four flow conditions at two streamwise locations. For the momentumless-wake case, the rapid decay of the mean shear is quite evident. For example, by $x/d = 45$ the centreline velocity difference, U_d, of the momentumless wake becomes less than 1% of the free-stream velocity. In other words, the mean velocity profile of the momentumless wake is almost flat at this distance downstream. The pure wake at this location has spread by almost a factor of two compared with the corresponding one at $x/d = 15$ while the momentumless wake has spread only slightly. These measurements are consistent with our earlier smoke-wire observations.

For the momentumless wake, the mean velocity profiles are normalized by the centreline velocity difference and the wake width l following convention. The centreline velocity difference, U_d, is defined as the absolute difference between free-stream velocity and mean centreline velocity. Lengthscale l is defined as the half-width of the streamwise turbulence intensity profile; this scale turns out to be more appropriate than that based on mean velocity profiles (see Naudascher 1965; Gran 1973; Higuchi 1977).

These profiles are plotted in figure 7 for $x/d = 5$ to 75. The profiles are self-similar, but this two-dimensional case has a much sharper profile than the axisymmetric momentumless wake profiles observed by Naudascher (1965) or Higuchi (1977). Normalized profiles for the pure wake, weak wake, and weak jet can be found in Park (1989).

Symmetry of the mean velocity profile was extremely sensitive to the angle of attack of the model. Thus, for accurate mean velocity measurements of the

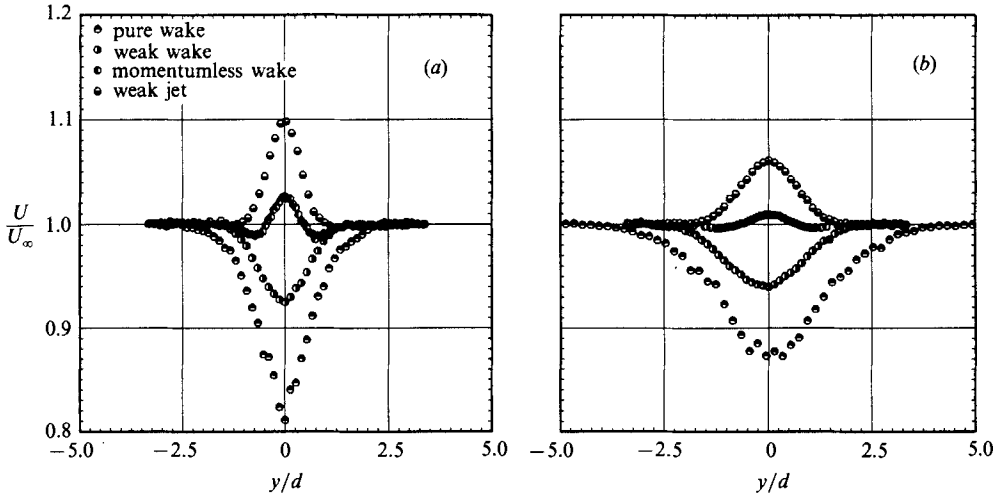

FIGURE 6. Mean velocity profiles at $Re = 5400$, and at (*a*) $x/d = 15$ and (*b*) 45.

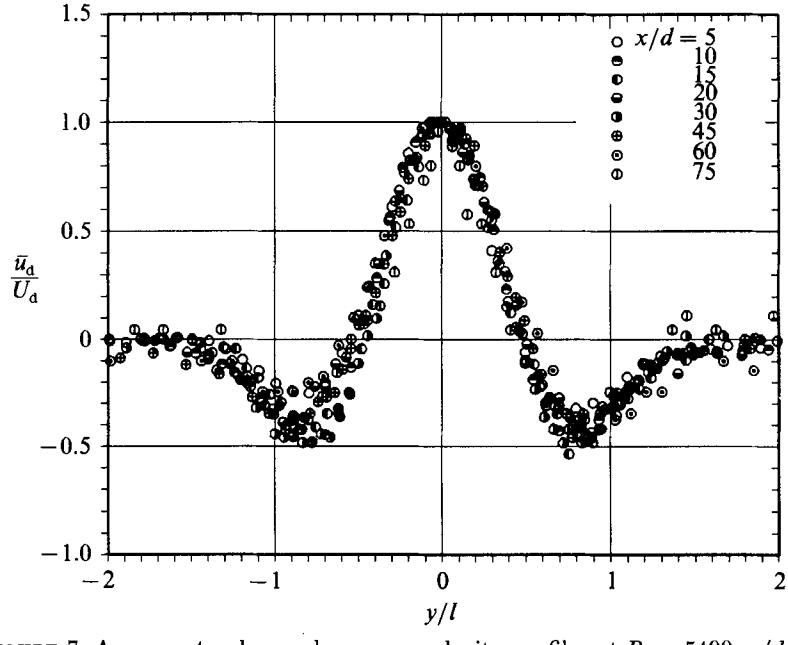

FIGURE 7. A momentumless wake: mean velocity profiles at $Re = 5400$, $x/d = 5$ to 75.

momentumless wake, it was necessary to align the model exactly parallel to the direction of the free stream. Because the bottom wall of the test section had a 0.5° slope downward from the inlet to the outlet, the model was aligned to half of this slope. This turned out to give the most symmetric profiles.

The decay of centreline velocity difference and the spreading rate of the momentumless wake are presented on a log-log scale in figure 8. The decay follows $U_d \sim x^{-0.92}$ which does not agree with the eddy-viscosity prediction ($x^{-0.75}$) of Tennekes & Lumley (1972). The spreading rates follows $l \sim x^{0.30}$ (figure 8), which again deviates from the prediction ($x^{0.25}$) of Tennekes & Lumley. For comparison, a

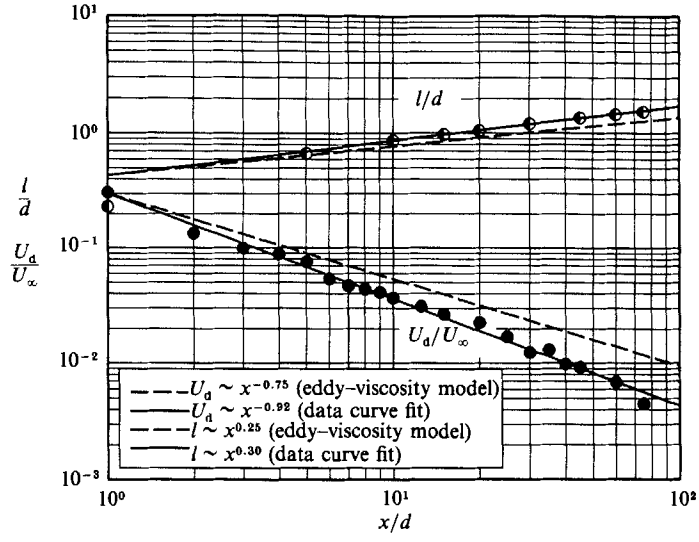

FIGURE 8. Rate of spreading and centreline velocity difference decay for the momentumless wake at $Re = 5400$.

$\frac{x}{d}$	$\frac{l}{d}$	$\frac{U_d}{U_\infty}$	$\frac{u'_{max}}{U_\infty}$	$\frac{v'_{max}}{U_\infty}$	$\frac{w'_{max}}{U_\infty}$	$\frac{\overline{u'v'}_{max}}{U_\infty^2} \times 10^2$	$\frac{\overline{q^2}_{max}}{U_\infty^2} \times 10^2$
1	0.23	0.306	0.370	0.317		5.420	17.199
5	0.67	0.080	0.090	0.098		0.269	1.225
10	0.86	0.036	0.054	0.053		0.089	0.416
15	0.97	0.026	0.039	0.037	0.034	0.040	0.211
20	1.05	0.022	0.032	0.030		0.026	0.137
30	1.20	0.012	0.022	0.020		0.014	0.069
45	1.35	0.0092	0.016	0.014	0.013	0.0054	0.034
60	1.46	0.0069	0.012	0.011		0.0026	0.021
75	1.54	0.0045	0.010	0.009		0.0020	0.014

TABLE 2. Summary of mean flow and turbulence quantities

pure wake follows $U_d \sim x^{-\frac{1}{2}}$ and $l \sim x^{\frac{1}{2}}$. Some characteristic values of the mean flow as well as the turbulent quantities are listed in table 2 for the momentumless wake.

4.2. *Turbulence measurements for the momentumless wake*

The mean velocity measurements show that the velocity profiles of our flow field are reasonably symmetric about the model centreline. Turbulence measurements for the momentumless wake at $Re = 5400$ were thus performed only for the upper half of the wake field. Instantaneous velocity components, u and v (or u and w after 90° rotation of the probe), were measured with an $\times$-wire probe with constant-temperature hot-wire anemometers. To reflect the effect of ambient temperature variation during measurement, the direct hot-wire calibration technique was utilized.

One-dimensional frequency spectra (based on the axial fluctuating velocity component u') for the pure wake and the momentumless wake at $Re = 5400$ were obtained from the single-sensor hot-wire data by performing an FFT on 4096 samples of u', sampled at 4 kHz; final smooth frequency spectra were then obtained

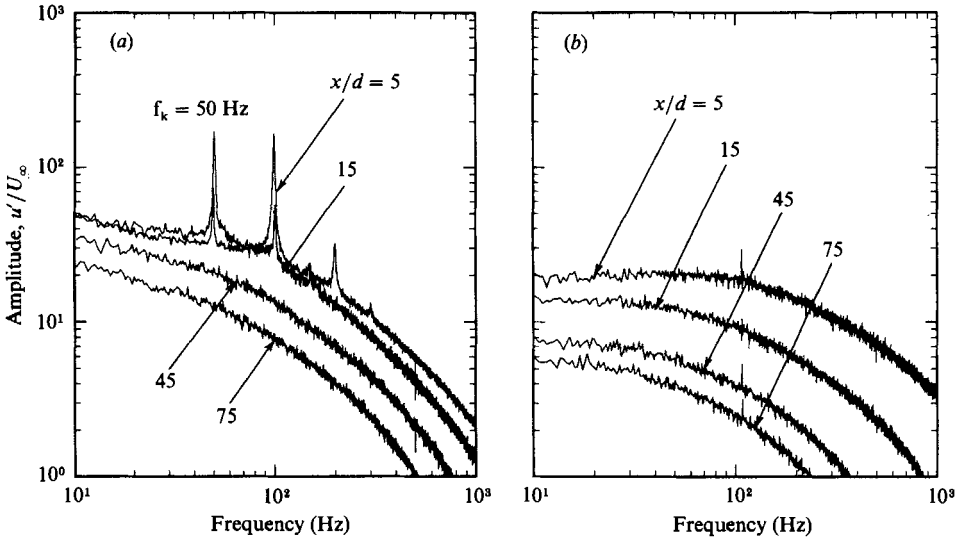

FIGURE 9. Frequency spectra at several downstream locations at $y/d = 0$ and at $Re = 5400$: (*a*) pure wake, (*b*) momentumless wake.

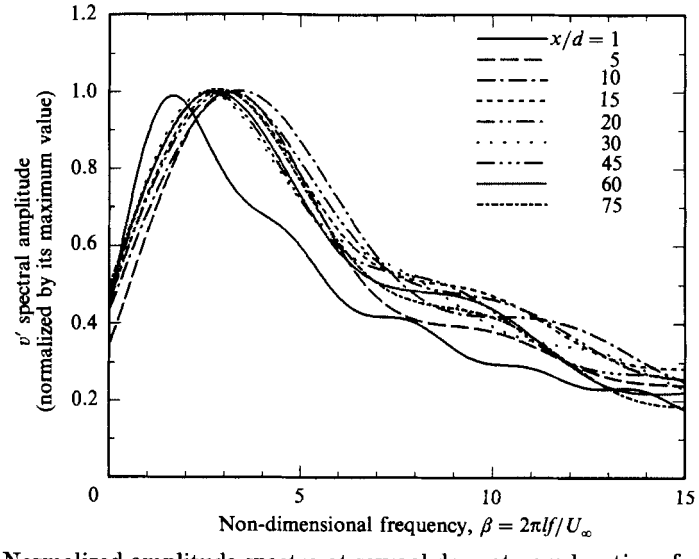

FIGURE 10. Normalized amplitude spectra at several downstream locations for the momentumless wake at $Re = 5400$. (y-locations were off the centreline: at the zero crossing of U profiles.)

by averaging the results of 100 such FFT's. As typical cases, spectra are plotted for $x/d = 5$, 15, 45 and 75 in figure 9. All of the spectra were measured at the y location where the r.m.s. fluctuating velocity peak occurred, i.e. at $y/d = 0$ for these particular stations. While a Kármán vortex shedding frequency ($f_{\text{peak}} \approx 50$ Hz) and its harmonics are clearly present for the pure-wake case in the near-wake region (figure 9*a*), there are no such identifiable peaks in the momentumless wake (figure 9*b*).

Additional spectral analysis was performed with the cross-wire data. Namely,

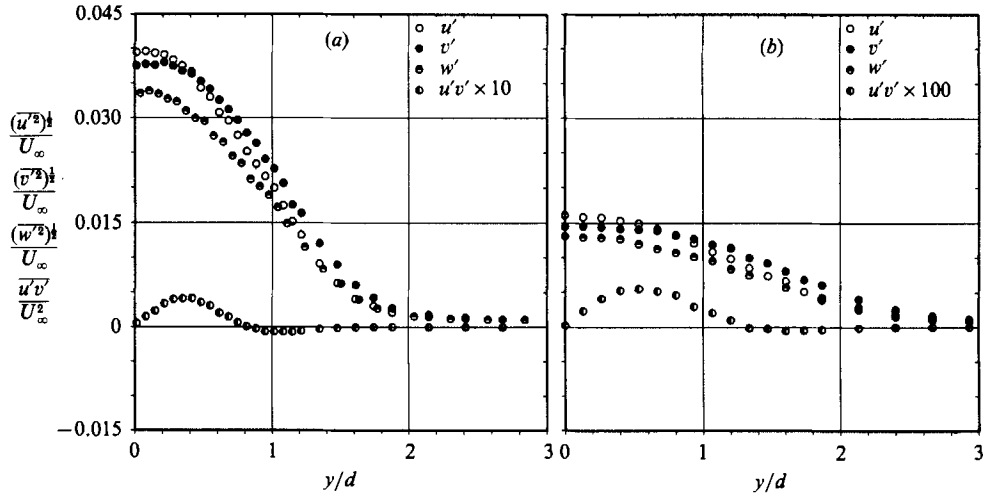

FIGURE 11. Axial, transverse and lateral turbulence intensities and Reynolds stress profiles for the momentumless wake at $Re = 5400$; (*a*) $x/d = 15$ and (*b*) 45.

amplitude spectra based on the transverse fluctuating velocity component, v', were obtained at several downstream locations and at y-locations where the local mean velocity between the primary and secondary extrema in the mean velocity profiles was the same as the free stream (i.e. near the edge of the momentumless wake). Figure 10 shows these amplitude spectra normalized in the usual manner; i.e.

$$\beta = \frac{2\pi l f}{U_\infty} \tag{4.2}$$

where f is the dimensional frequency, and l is the lengthscale for the momentumless wake discussed earlier. All the profiles have a peak at about the same non-dimensional frequency ($\beta \sim 3$) except for $x/d = 1$. This indicates that there exists a quasi-periodic vertical motion caused by some sort of large turbulence structure near the momentumless wake boundaries.

Axial turbulence intensity, $(\overline{u'^2})^{\frac{1}{2}}$, transverse turbulence intensity, $(\overline{v'^2})^{\frac{1}{2}}$, and Reynolds stress, $\overline{u'v'}$, along the model centreline were measured at nine streamwise stations from 1 to 75 diameters downstream of the model. At each sampling point, the instantaneous velocity components, u and v, were sampled and directly stored over a period of 20 s. All other mean quantities, such as pressures and temperatures, were sampled and integrated over 20 s, but only the final time-averaged values were stored. Typical profiles at $x/d = 15$ and $x/d = 45$ are shown in figures 11 (*a*) and 11 (*b*) respectively. Profiles at the other streamwise locations can be found in Park (1989).

At $x/d = 15$ (figure 11*a*), the axial intensity is slightly higher than the transverse intensity near the centre and somewhat lower further away from the centreline. The difference between the peak values of axial intensity and transverse intensity is about 5–10%. Note that this behaviour of our plane momentumless wake is quite different than that of the plane wake behind a flat plate observed by Chevray & Kovasznay (1969) or that of the plane jet observed by Bradbury (1965).

At $x/d = 45$ (figure 11*b*), both profiles become weak (flat and wide in shape); however, they retain the same relative behaviour. Namely, the maximum axial turbulence intensity is about 7–10% greater than the transverse intensity near the

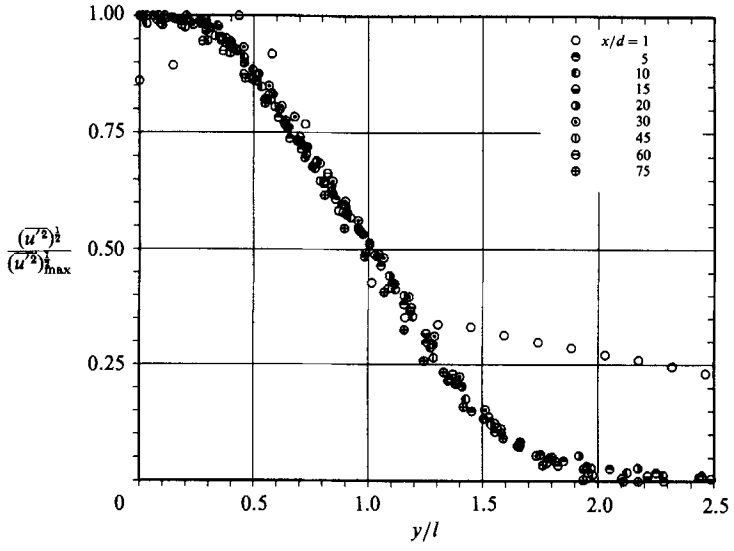

FIGURE 12. Normalized axial turbulence intensity profiles for the momentumless wake at $Re = 5400$, $x/d = 1$ to 75.

centreline, but the transverse intensity crosses over and is higher away from the centreline. This behaviour was observed at all streamwise locations except very near the body ($x/d \leqslant 10$).

The lateral, $(\overline{w'^2})^{\frac{1}{2}}$, turbulence intensity profiles measured at 15 and 45 diameters downstream are also shown in figures 11 (*a*) and 11 (*b*) respectively. At both stations, the profiles of the lateral turbulence intensity are similar to those of the axial ones, but about 10% lower in magnitude.

All of the axial intensity profiles are replotted in figure 12, with normalized coordinates, i.e. $(\overline{u'^2})^{\frac{1}{2}}/(\overline{u'^2})^{\frac{1}{2}}_{max}$ versus y/l. In this figure, overall similarity of the axial turbulence intensity appears to exist; the shape of the normalized profile is Gaussian-like except for the very near-wake station of $x/d = 1$. This non-dimensionalized axial turbulence intensity profile is virtually the same as that of the axisymmetric momentumless wakes (Naudascher 1965; Gran 1973; Higuchi 1977).

It was observed that the symmetry and overall shape of the turbulence intensity profiles are much less sensitive to small mismatches of momentum injection or small misalignment of the model than are the mean velocity profiles. In other words, bell-shaped and fairly symmetric profiles of turbulence intensities were still obtained with relatively large mismatches of momentum injection, although their maximum values were changed accordingly. With inappropriate alignments of the jet-injection model to the direction of free-stream, i.e. with some finite angle of attack, significantly distorted asymmetric mean velocity profiles were obtained; however, corresponding turbulence intensity profiles were fairly symmetric about the centreline. Thus, the existence of symmetric Gaussian-like turbulence intensity profiles does not always guarantee that the flow is in the momentumless state. For accurate investigation of momentumless wakes, therefore, the mean velocity profiles must not be overlooked, even though those flows usually relax towards a virtually flat profile quickly and thus the detailed survey of those profiles seems to be trivial.

The Reynolds stress profiles are also shown together with the turbulence intensity profiles in figures 11 (*a*) and 11 (*b*) for $x/d = 15$ and 45 respectively. Normalized

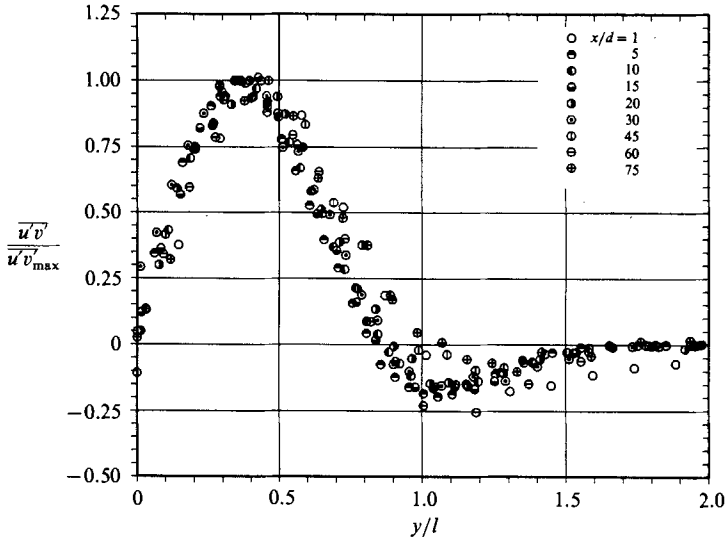

FIGURE 13. Normalized Reynolds stress profiles for the momentumless wake at $Re = 5400$, $x/d = 1$ to 75.

Reynolds stress profiles, $\overline{u'v'}/(\overline{u'v'})_{max}$ versus y/l, are shown in figure 13 for $x/d = 1$ to 75. Again, overall similarity in these profiles can be observed. This self-similar profile is very similar to that of the axisymmetric momentumless wake; the Reynolds stress at the centreline and the outer edge of the wake was zero, with positive and negative peaks occurring at $y/l \approx 0.4$ and at the wing of the profile ($y/l \approx 1.0$) respectively.

A negative region does not appear in the Reynolds stress profile of the pure wake (see Carmody 1964 for axisymmetric wake, and Chevray & Kovasznay 1969 for a two-dimensional wake) or the plane jet (Bradbury 1965). This is a unique feature of the momentumless wake due to the multiple inflection points in the mean velocity profile. In other words, the negative portion of the Reynolds stress profile of the momentumless wake is formed owing to the additional momentum flux injected into the wake field. It is of interest to note here that the amplitude of the negative region around $0.9 < y/l < 1.5$ is directly related to the symmetry of the flow. The shape of the negative region is much more sensitive to the angle of attack of the jet-injection model than that of the mean velocity profile. The Reynolds stresses are zero approximately at $y/l \approx 0.9$; this indicates that zero mean shear occurs quite close to the y/l position of the secondary extrema in mean velocity profiles ($y/l \approx 0.8$); however, these two are apparently not coincident.

The decay rates for the maximum turbulence intensities and shear stresses are plotted in figure 14. For both $(\overline{u'^2})^{\frac{1}{2}}_{max}$ and $(\overline{v'^2})^{\frac{1}{2}}_{max}$, the decay rate follows as $x^{-0.81}$ which is much faster than the two-dimensional pure wake ($x^{-\frac{1}{2}}$) or the plane jet ($x^{-\frac{1}{2}}$) but slightly slower than the axisymmetric momentumless wake (x^{-1}) observed by Naudascher (1965). Notice that the decay rate of $(\overline{u'^2})^{\frac{1}{2}}_{max}$ differs significantly from that of the mean centreline velocity defect, U_d (see figure 8). Namely, U_d decays faster ($x^{-0.92}$) than does $(\overline{u'^2})^{\frac{1}{2}}_{max}$ ($x^{-0.81}$). This observation explains why simple turbulence models such as constant eddy-viscosity and mixing-length models are inappropriate for prediction of momentumless wakes.

Based on our measurements, the decay rate for $(\overline{u'v'})_{max}$ ($x^{-1.84}$) turned out to be

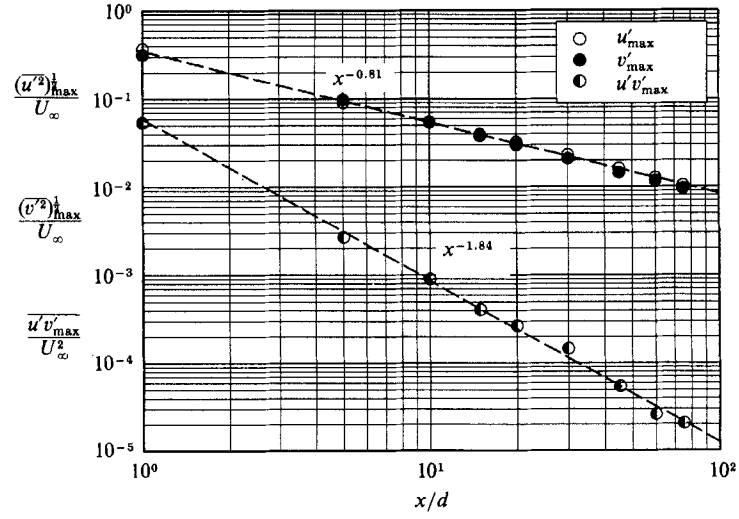

FIGURE 14. Decay of the maximum axial and transverse turbulence intensities and the Reynolds stress for the momentumless wake at $Re = 5400$.

the same as the square of the decay rate for U_d, but the former is much faster than that of the square of the maximum axial turbulent intensity. For comparison, the decay rates both for $\overline{u'v'_{max}}$ and $\overline{u'^2_{max}}$ are the same as that of U_d^2 for elementary free-shear flows (see for example Naudascher 1965 or Tennekes & Lumley 1972). We can, thus, consider our two-dimensional momentumless wake as nearly isotropic turbulence, at least beyond some distance (say, 45 body diameters) from the wake generator.

Finally, the normalized turbulent kinetic energy profiles for the momentumless wake at $x/d = 1$ to 75 are presented in figure 15. Here, the turbulent kinetic energy is defined as $\overline{q^2} = \frac{1}{2}[\overline{u'^2} + \overline{v'^2} + \overline{w'^2}]$ and the magnitude of w' is assumed to be $0.9u'$ based on our observations at $x/d = 15$ and 45, as discussed above. Here $\overline{q^2}$ is normalized by its maximum value, and y by a new lengthscale, l^*, where l^* is the distance between the centreline of the flowfield and the position where the local $\overline{q^2}$ is half the maximum $\overline{q^2}$. It is expected that these profiles would be fit with a Gaussian error function (Naudascher 1965); however, the present profiles have a slightly sharper bell shape than the axisymmetric momentumless-wake case observed by Naudascher (1965). It is conjectured that our plane wake has more vigorous mixing near the centre region, but beyond $y/l^* > 1.0$ turbulent kinetic energy is damped out more quickly to the free-stream level. The spreading rate of the turbulent kinetic energy lengthscale l^* for the momentumless wake turned out to be $l^* \sim x^{0.35}$, which is slightly faster than that of l ($x^{0.3}$).

5. Three-dimensional effects

Let us now discuss three-dimensionality of our two-dimensional pure wake and momentumless wake. For far wakes of two-dimensional cylinders, it is known that there exist unique patterns of three-dimensional structure although the mechanism responsible for these patterns is not completely understood (Grant 1958; Roshko 1976; Cimbala *et al.* 1988).

To investigate the three-dimensional structure, flow visualizations were performed

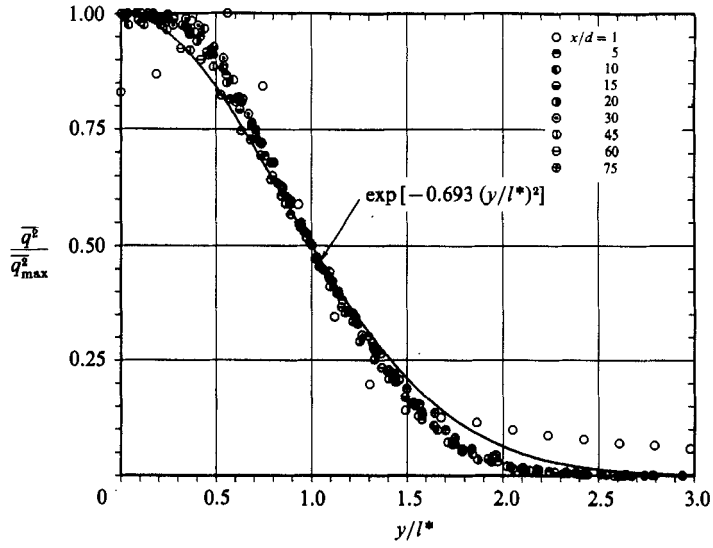

FIGURE 15. Normalized turbulent kinetic energy profiles for the momentumless wake at $Re = 5400$, $x/d = 1$ to 75.

by turning the test section of our wind tunnel 90° to obtain plan views, while keeping the smoke wire vertical. Figures 16 and 17 show both edge (x, y-plane) and plan (x, z-plane) views of the pure wake and momentumless wake respectively at $Re = 5400$. (The two views were taken for the same tunnel conditions and air jet-injection conditions, though not simultaneously.) For the edge views, the smoke wire was positioned at $x/d = 0$, 15, 30 and 45 in the manner discussed previously. For the plan views, the smoke wire was at $x/d = 3$, 15, 30 and 45, but at $y/d = 0$ (i.e. in the centreplane of the wakes), and parallel to the model.

For the pure wake, as seen in figure 16, the edge view shows the Kármán vortex street and the subsequent growth of secondary structure. In the plan views, particularly photograph (*b*), some crescent-shaped structures can be seen, similar to those observed by Cimbala *et al.* (1988) at lower Reynolds number.

In contrast with the pure-wake case, the momentumless wake shows no such organized three-dimensional structure (figure 17). Instead, the plane view of photograph (*a*) illustrates somewhat homogeneously dispersed small-scale turbulence in the (x, z)-plane. The plan views of photographs (*b–d*) show progressively the decay of such small-scale turbulence. Beyond 45 body diameters (photograph *d*), the momentumless wake is well on its way to relaminarization.

One of the most interesting features of the momentumless wake can be detected at the interface between the highly turbulent core region and the non-turbulent free-stream region. As discussed earlier, turbulent structures which are neither wake-like nor jet-like randomly burst out into the free stream; these bursts can be clearly seen particularly in the edge view of photograph (*b*) in figure 17. To further investigate these bursts in the momentumless wake as well as the three-dimensional structure in the pure wake, additional plan views were taken with the smoke wire at y-locations off the centreplane.

In figure 18, plan views of the pure wake and momentumless wake at $Re = 5400$ are visualized with the smoke wire at $x/d = 15$ and at $y/d = 1.33$, i.e. near the momentumless wake boundary (off the centreplane). For the pure-wake case

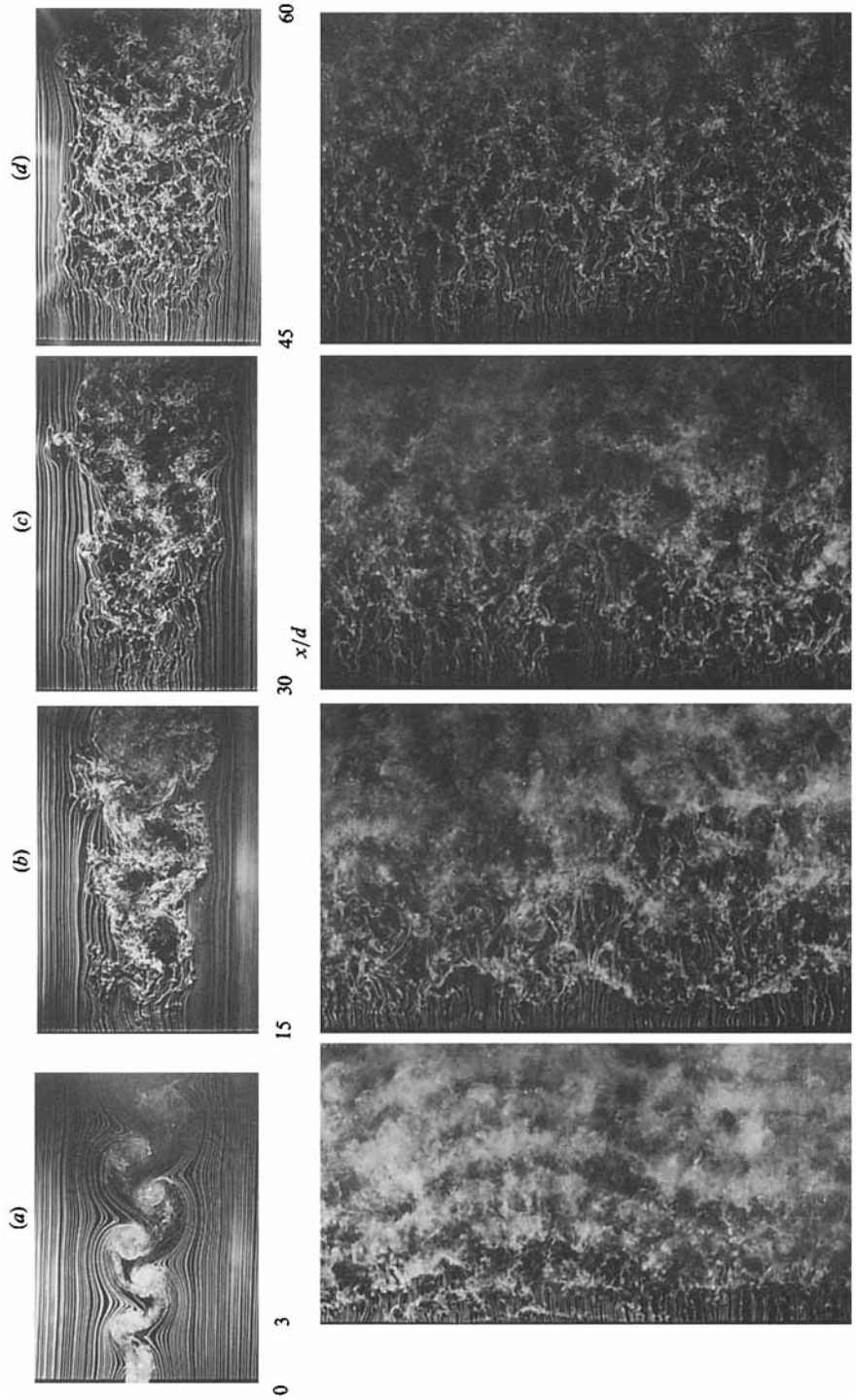

FIGURE 16. Edge and plan views of a pure wake at $Re = 5400$; smoke wire at (*a*) $x/d = 0$ or 3, (*b*) 15, (*c*) 30, and (*d*) 45; and at $y/d = 0$.

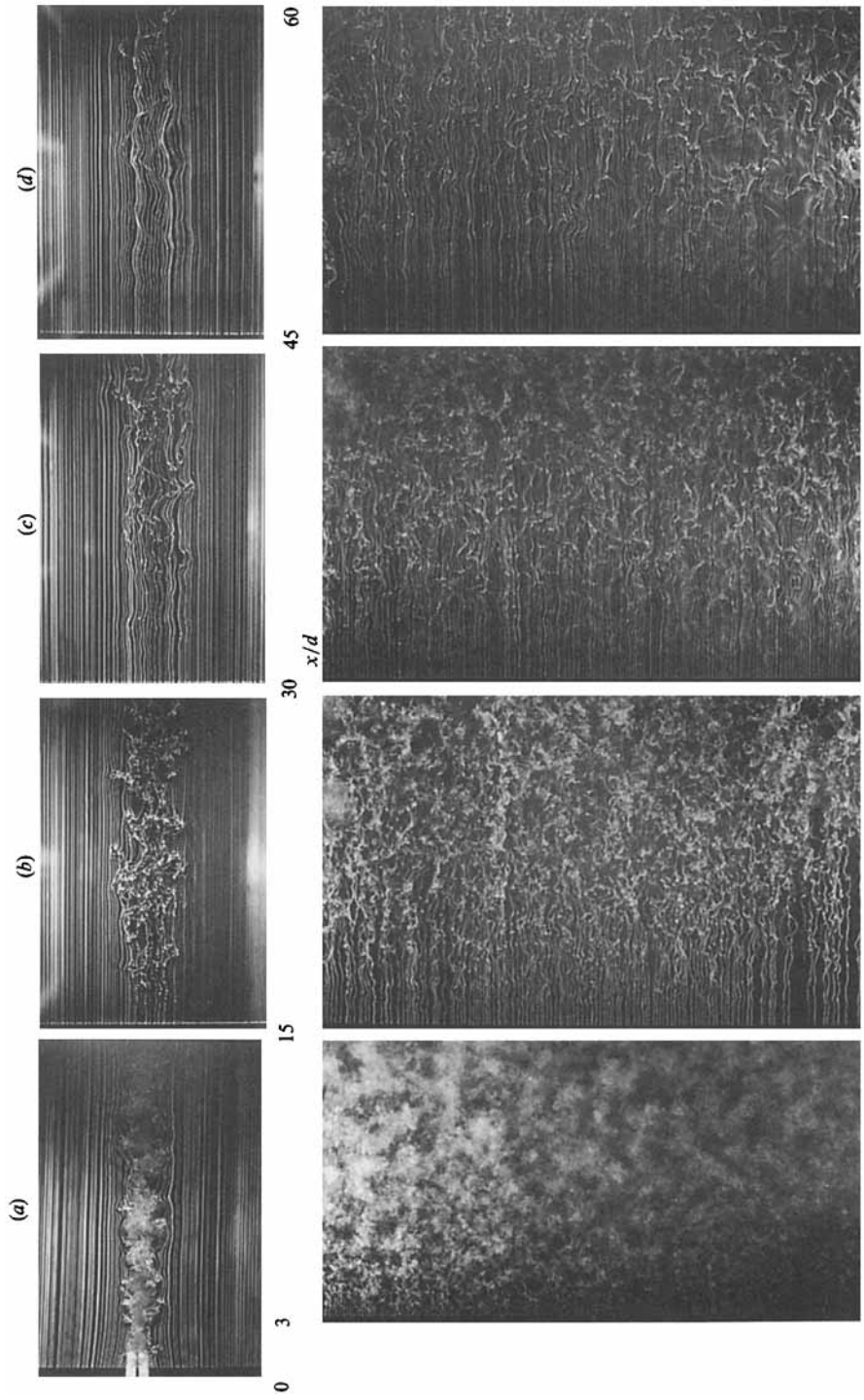

FIGURE 17. Edge and plan views of a momentumless wake at $Re = 5400$; smoke wire at (*a*) $x/d = 0$ or 3, (*b*) 15, (*c*) 30, and (*d*) 45; and at $y/d = 0$.

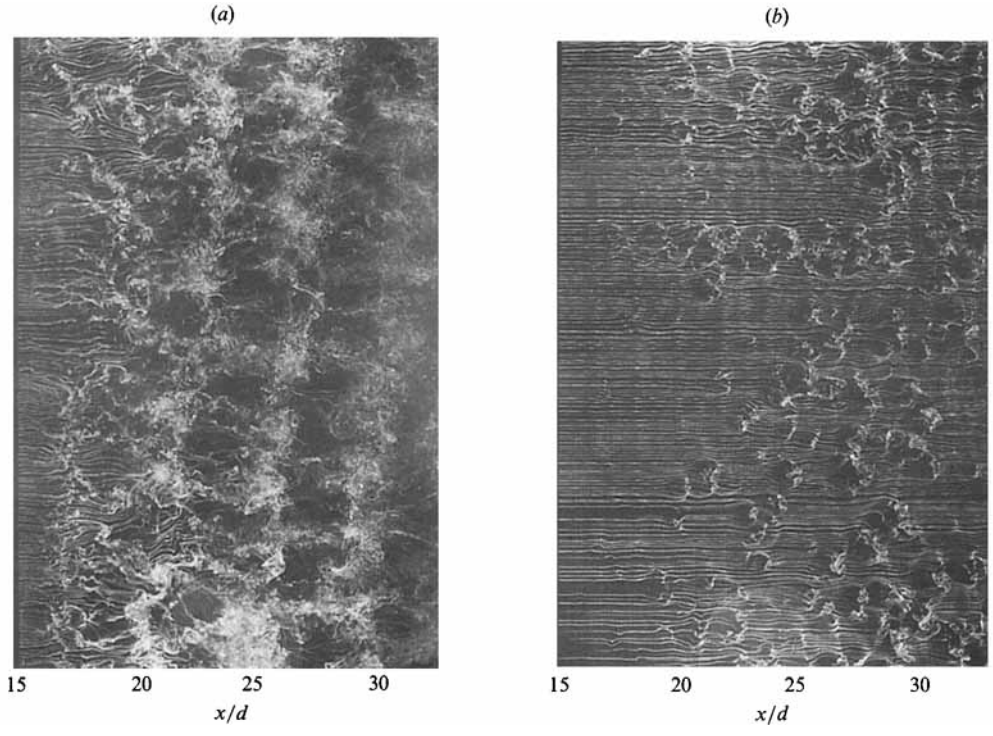

FIGURE 18. Plan view of (*a*) a pure wake and (*b*) a momentumless wake at $Re = 5400$; smoke wire at $x/d = 15$, $y/d = 1.33$.

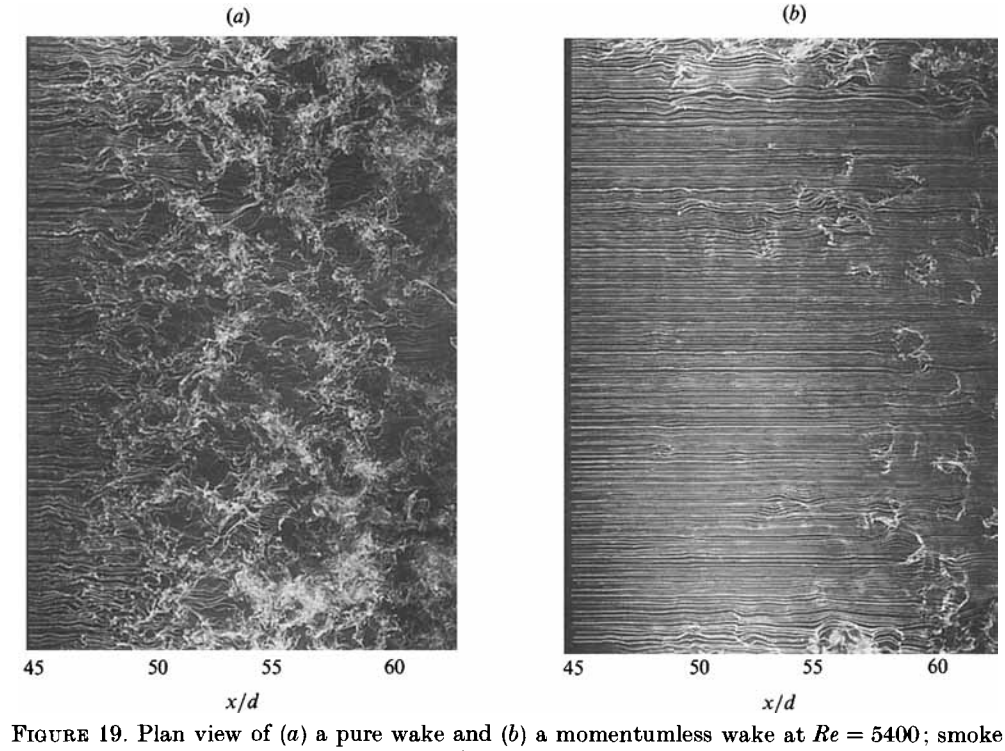

FIGURE 19. Plan view of (*a*) a pure wake and (*b*) a momentumless wake at $Re = 5400$; smoke wire at $x/d = 45$, $y/d = 2.0$.

(photograph *a*), the three-dimensional wavy structures are more clearly observed compared with figure 16. The momentumless-wake case (photograph *b*) reveals that individual bursts are heart-shaped and isolated in the spanwise direction. These bursts in the (x, z)-plane are about a body diameter in size at this specific downstream location. In the middle upper half of photograph (*b*), many of these bursts are clustered on the same line in the x-direction. This was observed in 10 out of 12 photographs, and is believed to be the result of a non-uniformity in our jet-injection model. However, the other three-dimensional structures occur randomly in the spanwise direction; the observed heart-shaped bursts are therefore thought to be inherent features of the flow field.

Similarly, figure 19 shows plan views of the pure wake and the momentumless wake far downstream (at $x/d = 45$ to 60 and at $y/d = 2.0$). Again, the growth in scale of the characteristic structures can be more clearly observed. The three-dimensional structure, although still discernible, becomes more disorganized for the pure wake (photograph *a*). The number of bursts is reduced for the momentumless wake (photograph *b*) compared with the corresponding structures at $x/d = 15$ to 30 (figure 18*b*) while the size of individual bursts is increased somewhat. Notice the large disturbances at the top and bottom of photograph (*b*) at this far downstream location. This is due to end effects from our jet-injection model. (Recall that the air injection slit covers only about 80% of the total model span.) These photographs verify that end effects are not significant at the centreline (where all our hot-wire measurements were taken), even at the furthest downstream locations.

6. Discussion and conclusions

The rapid decay of turbulence structures downstream of the two-dimensional momentumless body was studied by flow visualizations as well as hot-wire measurements. The decay rate of the centreline velocity difference was found to be much faster than that of the pure wake or pure jet. Consequently, fast decay of the mean shear was also observed; this flow is thus analogous to grid turbulence at least beyond a certain distance from the body, i.e. beyond $x/d \approx 45$.

The present spreading rate of the momentumless wake is compared (figure 20) with the rates observed by Townsend (1956) and Mobbs (1968) for their two-dimensional inhomogeneous turbulence flows with plane geometry. The spreading rate of Townsend's integral lengthscale L based on the axial turbulent intensity profile was about $x^{0.8}$, which is even faster than that of the analytical prediction for the two-dimensional pure wake ($x^{0.5}$). Mobbs reported the variation of the scale of the intermittent zone L_γ with distance x from his composite grid and compared with the lengthscale L observed by Townsend. He interpreted his data by assuming that the self-preservation of intensity distributions is a consequence of the self-preservation of the intermittency factor distribution; the length scale L_γ beyond some downstream distance ($x \sim 120$ cm) should therefore follow the same spreading rate as Townsend's lengthscale L. The last three data points of Mobbs in figure 20 do appear to following Townsend's data, as pointed out by Mobbs. However, Mobbs' data taken as a whole may instead be interpreted as following the same growth rate ($x^{0.3}$) as the present measurements (indicated by the dashed line). It is not clear why Townsend's spreading rate is so large.

The present decay rate of the axial turbulence intensity ($x^{-0.81}$) is much faster than that of Townsend (1956). Townsend suggested that the rate of decay of turbulence intensity in his shear-free inhomogeneous flow was rather more rapid than that of

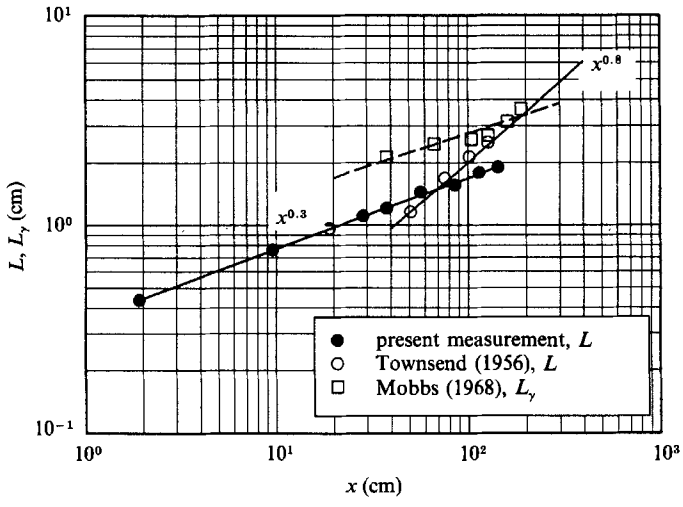

FIGURE 20. Rate of spreading of two-dimensional momentumless wakes.

$$L = \left[\int_{-\infty}^{\infty} \overline{u'^2} y^2 \, dy \Big/ \int_{-\infty}^{\infty} \overline{u'^2} \, dy\right]^{\frac{1}{2}}$$

$$L_\gamma = \left[\int_{-\infty}^{\infty} \gamma y^2 \, dy \Big/ \int_{-\infty}^{\infty} \gamma \, dy\right]^{\frac{1}{2}}, \quad \gamma = \text{intermittency factor.}$$

isotropic turbulence; his integral velocity scale decayed as $x^{-0.55} - x^{-0.6}$ while that of isotropic turbulence decays as $x^{-0.5}$ (Batchelor 1953).

As discussed earlier, a unique large-scale turbulence structure was observed in our two-dimensional momentumless wake. Namely, bursts of turbulent structures were observed near the boundary of the momentumless wake. Although large-scale bursts of this type have been reported by Higuchi (1977), and Gilreath & Brandt (1983) for their axisymmetric momentumless wakes, the driving mechanism which triggers this phenomenon is still unknown. We may thus raise the following questions: (1) Under what conditions can this peculiar large-scale turbulence structure be formulated? (2) How is this unique structure related to the experimentally observed very rapid decay of the momentumless wake? Some suggestions are proposed here based on our flow-visualization observations and supported by our spectral measurements.

Since the momentumless wake is a combination of a wake and a jet, vortical structures from both of these will be present. For example, in the upper half of the flow field, clockwise vortices created by the wake will interact with counterclockwise vortices created by the jet. After numerous active interactions (such as cancellation and amalgamation) of these vortices, some individual vortices may survive and convect downstream. Two such vortices of opposite sign but nearly equal strength can then form a vortex pair which drives itself towards the free stream. Presumably, the characteristic frequency of this bursting depends on the frequency of the wake-like structures and that of the jet-like structures, and perhaps on the mismatch or phase jitter between the two. Spanwise coherence of these bursts is not expected since the pure wake itself is highly three-dimensional. Analysis of several photographs like those of figures 18 and 19 indicates that there seems to be a tendency for the bursts to occur quasi-periodically on a given line in the streamwise direction rather than in a totally random manner. This may be related to the relative frequencies of

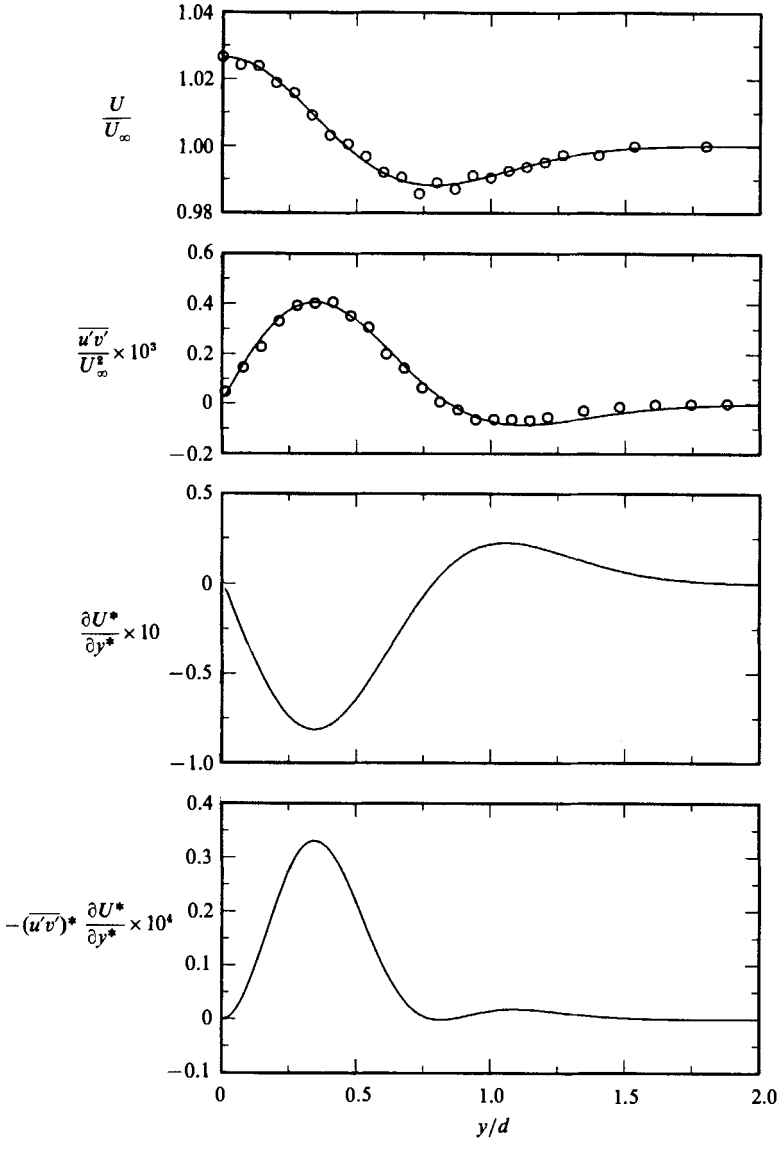

FIGURE 21. Local production for the momentumless wake at $Re = 5400$ and at $x/d = 15$.
$U^* = U/U_\infty, y^* = y/d, (\overline{u'v'})^* = (\overline{u'v'})/U_\infty^2$.

the wake and jet as conjectured above. Non-uniformities in the jet may also contribute to this behaviour.

Spectra of the fluctuating transverse velocity show a prominent broad band of energy centred around non-dimensional frequency $\beta \approx 3$, as was shown in figure 10. At $x/d = 15$, for example, this corresponds to a dimensional frequency of about 80 Hz. From photograph (*b*) of figure 18 one can estimate the frequency of consecutive bursts by following lines in the streamwise direction. The frequency determined in this manner ranges from about 40 to 120 Hz, with an average value which is also near 80 Hz; thus the prominent band of spectral energy appears to be related to these structures which burst out into the free stream.

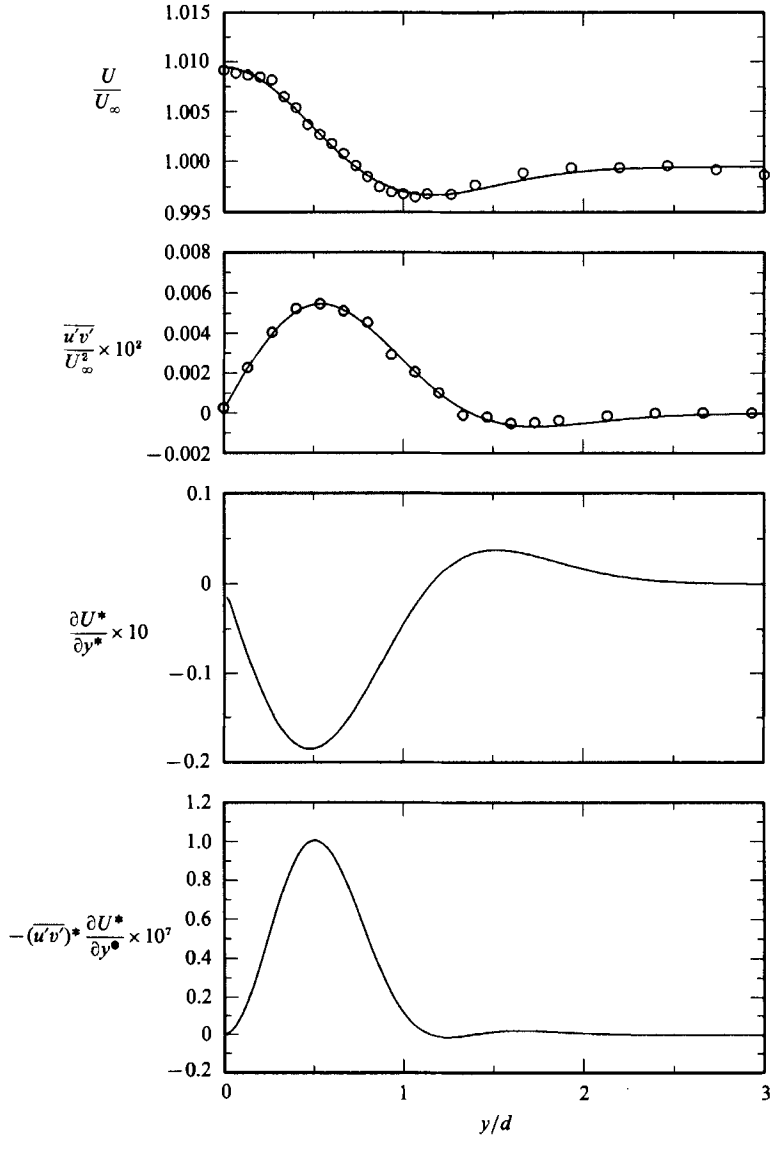

FIGURE 22. Local production for the momentumless wake at $Re = 5400$ and at $x/d = 45$.

Once the turbulent structure puffs outward, no more turbulent energy can be furnished because the mean shear changes its sign near the edge of the wake and becomes negligibly small downstream in the momentumless wake. Consequently, this turbulence bulge is isolated from the main bulk of the turbulence flow, evolves in the isolated spot, and finally relaminarizes after losing its turbulence energy completely by dissipation. On the other hand, the main bulk of turbulence flow loses some of its turbulence energy each time it ejects one of these bulges. This is in addition to the ordinary gradient diffusion processes. In other words, the governing mechanism for the fast decay of turbulence in the momentumless wake may not be due purely to gradient diffusion (cf. Wang 1965 and Naudascher 1965). Instead, two additional mechanisms are at work here. Namely, interaction (i.e. cancellation) of the jet-like and wake-like vortices, and the ejection of turbulent bursts into the free stream.

From the flow visualizations in figures 18 and 19, we can find partial justification for our proposal, i.e. the decrease in the number of bursting events. Among the turbulent eddies which were formulated in the near-wake region, only a few can survive and convect downstream to eventually form these bursts. The decrease in the number of bursts with downstream distance is consistent with these arguments.

For two-dimensional free-shear flows, production in the turbulent energy equation can be expressed as the product of Reynolds stress and mean axial velocity gradient (Tennekes & Lumley 1972), i.e.

$$P = -\overline{u'v'}\frac{\partial U}{\partial y} \tag{6.1}$$

Typical profiles of local turbulence production at $x/d = 15$ and 45 are plotted in figures 21 and 22 respectively. To differentiate U, a smooth curve was first fit to the data to avoid large numerical inaccuracies. Notice that the maximum local production becomes of order 10^{-7} (i.e. negligibly small) at $x/d = 45$. It is interesting to note that production for the momentumless wake is quite different in shape than that of the pure wake. Namely, present production profiles have a negative region (although quite small in magnitude) around the secondary extrema in the mean velocity profiles. This negative region (i.e. region of local destruction of turbulence) segregates the wake into two parts with opposite signs of mean shear. In non-zero-drag wakes, production and dissipation in the turbulence energy budget are roughly in equilibrium, i.e. $P \sim U_d(u'_{max})^2/l$ and $\epsilon \sim (u'_{max})^3/l$ are of the same order of magnitude. In the momentumless wake, however, U_d decays much faster than u'_{max} and thus the balance between production and dissipation no longer exists shortly after some distance downstream. This is the more specific reason why simple turbulence models fail to predict this flow. As a consequence, some higher-order turbulence models (e.g. a second-order Reynolds stress model), which can, at least, handle production and dissipation individually, should be applied for reasonable prediction of the momentumless wake.

In summary, it has been experimentally verified that the unique property of this flow field, which distinguishes it from jets, wakes and mixing layers, is the very rapid decay of turbulence due to lack of production of turbulent energy. The set of experimental data reported here is expected to be quite useful for future developments of turbulence models.

On a final note, some very recent experiments by the authors suggest that the momentumless wake is extremely sensitive to model geometry. These experiments will be reported at a later date.

The authors are grateful for the financial support of the Engineering Foundation, USA, under Grant No. RI-A-86-6, and the National Science Foundation, USA, Grant No. MSM-8707653.

REFERENCES

BATCHELOR, G. K. 1953 *The Theory of Homogeneous Turbulence*, pp. 132–138. Cambridge University Press.

BEARMAN, P. W. 1966 Investigation into the effect of base bleed on the flow behind a two-dimensional model with a blunt trailing edge. *AGARD Conf. Proc.* No. 4, pp. 479–507.

BIRKHOFF, G. & ZARANTONELLO, E. H. 1957 *Jets, Wakes, and Cavities*. Academic. 1957.

BRADBURY, L. J. S. 1965 The Structure of a self-preserving turbulent plane jet. *J. Fluid Mech.* **23**, 31–64.

CARMODY, T. 1964 Establishment of the wake behind a disk. *Trans. ASME* D: *J. Basic Eng*, **86**, 869–880.

CHEVRAY, R. & KOVASZNAY, L. S. J. 1969 Turbulence measurements in the wake of a thin flat plate. *AIAA J.* **7**, 1641–1643.

CHIENG, C. C., JAKUBOWSKI, A. K. & SCHETZ, J. A. 1974 Investigation of the turbulent properties of the wake behind self-propelled, axisymmetric bodies. *VPI-Aero*-025, Sept. 1974.

CIMBALA, J. M. 1984 Large structure in the far wakes of two-dimensional bluff bodies. Ph.D. thesis, California Inst. of Technology.

CIMBALA, J. M., NAGIB, H. M. & ROSHKO, A. 1988 Large structure in the far wakes of two-dimensional bluff bodies. *J. Fluid Mech.* **190**, 265–298.

CIMBALA, J. M. & PARK, W. J. 1989*a* Elimination of temperature stratification in a low-speed open-return wind tunnel. *AIAA J.* **27**, 823–825.

CIMBALA, J. M. & PARK, W. J. 1989*b* A direct hot-wire calibration technique to account for ambient temperature drift in incompressible flow. *Exp. Fluids* (to appear).

DONALDSON, C. DU P. 1972 Calculation of turbulent shear flows for atmospheric and vortex motions. *AIAA J.* **10**, 4–12.

FINSON, M. L. 1975 Similarity behavior of momentumless turbulent wakes. *J. Fluid Mech.* **71**, 465–479.

GILREATH, H. E. & BRANDT, A. 1983 Experiments on the generation of internal waves in a stratified fluid. *AIAA Paper* 83–1704.

GINEVSKII, A. S., POCHKINA, K. A. & UKHANOVA, L. N. 1966 Propagation of turbulent jet flow with zero excess impulse. *Izv. Akad. Nauk. SSSR Mekh. Zhid. i Gaza* **1**, 164–166 (in *Fluid Dyn.* 1967, pp. 106–107, Faraday Press).

GINEVSKII, A. S., UKHANOVA, L. N. & POCHKINA, K. A. 1972 Turbulent co-flows with zero excess momentum. *Fluid Mech. Soviet Res.* **1**, 81–86.

GRAN, R. L. 1973 An experiment on the wake of a slender propeller-driven body. *Rep.* 20086-6006-RU-00, June 1973. TRW Systems.

GRANT, H. L. 1958 The large eddies of turbulent motion. *J. Fluid Mech.* **4**, 149–198.

HANJALIC, K. & LAUNDER, B. E. 1972 A Reynolds stress model of turbulence and its application to thin shear flows. *J. Fluid Mech.* **52**, 609–638.

HASSID, S. 1980 Similarity and decay law of momentumless wakes. *Phy. Fluids* **23**, 404–405.

HIGUCHI, H. 1977 Experimental investigation on axisymmetric turbulent wakes with zero momentum defect, Ph.D. thesis, California Inst. of Technology.

KO, D. R. S. 1973 A phenomenological model for the momentumless turbulent wake in a stratified medium. *Rep.* 20086-6007-RU-00, Apr. 1973. TRW Systems.

KOROBKO, V. I. & SHASHMIN, V. K. 1985 Dynamics and heat transfer of a turbulent and laminar momentumless wake. *Heat Transfer Soviet Res.* **17**, 96–103.

KUBOTA, T. 1975 Turbulent wake behind a self-propelled body, *Rep.* GALCIT-138, California Inst. of Tech.

LEWELLEN, W. S., TESKE, M. & DONALDSON, C. DU P. 1973 Application of turbulence model equations to axisymmetric wakes. *AIAA Paper* 73-648.

LEWELLEN, W. S., TESKE, M. & DONALDSON, C. DU P. 1974 Turbulent wakes in a stratified fluid, *Aero Res. Associates of Princeton, Rep.* 226, Aug. 1974.

LOEHRKE, R. I. & NAGIB, H. M. 1972 Experiments on management of freestream turbulence. *AGARD-R*-598.

METCALFE, R. W. & RILEY, J. J. 1981 Direct numerical simulations of turbulent shear flows. In *Proc. 7th Intl Conf on Numerical Methods in Fluid Dynamics*, pp. 279–284.

MOBBS, F. R. 1968 Spreading and contraction at the boundaries of free turbulent flows. *J. Fluid Mech.* **33**, 227–239.

NAUDASCHER, E. 1965 Flow in the wake of self-propelled bodies and related sources of turbulence. *J. Fluid Mech.* **22**, 625–656.

ORSZAG, S. A. & PAO, Y. H. 1973 Numerical computation of turbulent shear flows. *Flow Research Rep.* **19**, July 1973. Flow Research Inc.

PARK, W. J. 1989 An experimental investigation of the turbulent structure in two-dimensional momentumless wakes. Ph.D. thesis. The Pennsylvania State University.

RIDJANOVIC, M. 1963 Wake with zero change of momentum flux. Ph.D. thesis, State University of Iowa.

ROSHKO, A. 1954 On the development of turbulent wakes from vortex streets. *NACA Rep.* 1191.

ROSHKO, A. 1976 Structure of turbulent shear flows: a new look. *AIAA J.* **14**, 1349–1357.

ROTTA, J. 1951 Statistische Theorie Nichthomogener Turbulenz. *Z. Phys.* **129**, 547.

SCHETZ, J. A. 1980 Injection and mixing in turbulent flow. *Prog. Astronaut. Aeronaut.* **68**, 97–109.

SCHETZ, J. A. & JAKUBOWSKI, A. K. 1975 Experimental studies of the turbulent wake behind self-propelled slender bodies. *AIAA J.* **13**, 1568–1575; also *AIAA Paper* 75-117, 1975.

SCHETZ, J. A. & STANLEY, F. 1972 Analysis of free turbulent mixing flows without a net momentum defect. *AIAA J.* **10**, 1524–1526.

SHASHMIN, V. K. 1983 Hydrodynamics and heat exchange in turbulent momentumless wakes. *Engng Phys.* **44**, 438–442.

SWANSON, R. C., SCHETZ, J. A. & JAKUBOWSKI, A. K. 1974 Turbulent wake behind slender bodies including self-propelled configurations. *VPI- Aero*-024, Sept. 1974. Virginia Polytechnic Inst. and State University.

TENNEKES, H. & LUMLEY, J. L. 1972 *A First Course in Turbulence.* MIT Press.

TOWNSEND, A. A. 1956 *The Structures of Turbulent Shear Flow*, 1st edn., pp. 49–56. Cambridge University Press.

WANG, H. 1965 Flow behind a point source of turbulence. Ph.D. thesis, State University of Iowa.

WILLIAMS, D. R. & AMATO, C. W. 1988 Unsteady pulsing of cylinder wakes. *1st Natl Fluid Dynamics Congr., Cincinnati, Ohio, July 25–28.*

WOOD, C. J. 1964 The effect of base bleed on a periodic wake. *J. R. Aero. Soc. Tech. Notes* **68**, 477–482.

WOOD, C. J. 1967 Visualization of an incompressible wake with base bleed. *J. Fluid Mech.* **29**, 259–272.